Astronomy & Astrophysics

The *Gaia*-ESO survey: the non-universality of the age–chemical-clocks–metallicity relations in the Galactic disc[⋆,⋆⋆]

G. Casali[1,2], L. Spina[3,18], L. Magrini[2], A. I. Karakas[3,18], C. Kobayashi[4], A. R. Casey[3,18], S. Feltzing[15],
M. Van der Swaelmen[2], M. Tsantaki[2], P. Jofré[11], A. Bragaglia[12], D. Feuillet[15], T. Bensby[15], K. Biazzo[16],
A. Gonneau[5], G. Tautvaišienė[17], M. Baratella[7], V. Roccatagliata[2,8,25], E. Pancino[2], S. Sousa[9], V. Adibekyan[9],
S. Martell[19,18], A. Bayo[24], R. J. Jackson[23], R. D. Jeffries[23], G. Gilmore[5], S. Randich[2], E. Alfaro[14], S. E. Koposov[6],
A. J. Korn[21], A. Recio-Blanco[22], R. Smiljanic[20], E. Francisini[2], A. Hourihane[5], L. Monaco[10], L. Morbidelli[2],
G. Sacco[2], C. Worley[5], and S. Zaggia[13]

(Affiliations can be found after the references)

ABSTRACT

Context. In the era of large spectroscopic surveys, massive databases of high-quality spectra coupled with the products of the *Gaia* satellite provide tools to outline a new picture of our Galaxy. In this framework, an important piece of information is provided by our ability to infer stellar ages, and consequently to sketch a Galactic timeline.

Aims. We aim to provide empirical relations between stellar ages and abundance ratios for a sample of stars with very similar stellar parameters to those of the Sun, namely the so-called solar-like stars. We investigate the dependence on metallicity, and we apply our relations to independent samples, that is, the *Gaia*-ESO samples of open clusters and of field stars.

Methods. We analyse high-resolution and high-signal-to-noise-ratio HARPS spectra of a sample of solar-like stars to obtain precise determinations of their atmospheric parameters and abundances for 25 elements and/or ions belonging to the main nucleosynthesis channels through differential spectral analysis, and of their ages through isochrone fitting.

Results. We investigate the relations between stellar ages and several abundance ratios. For the abundance ratios with a steeper dependence on age, we perform multivariate linear regressions, in which we include the dependence on metallicity, [Fe/H]. We apply our best relations to a sample of open clusters located from the inner to the outer regions of the Galactic disc. Using our relations, we are able to recover the literature ages only for clusters located at $R_{GC} > 7$ kpc. The values that we obtain for the ages of the inner-disc clusters are much greater than the literature ones. In these clusters, the content of neutron capture elements, such as Y and Zr, is indeed lower than expected from chemical evolution models, and consequently their [Y/Mg] and [Y/Al] are lower than in clusters of the same age located in the solar neighbourhood. With our chemical evolution model and a set of empirical yields, we suggest that a strong dependence on the star formation history and metallicity-dependent stellar yields of s-process elements can substantially modify the slope of the $[s/\alpha]$–[Fe/H]–age relation in different regions of the Galaxy.

Conclusions. Our results point towards a non-universal relation $[s/\alpha]$–[Fe/H]–age, indicating the existence of relations with different slopes and intercepts at different Galactocentric distances or for different star formation histories. Therefore, relations between ages and abundance ratios obtained from samples of stars located in a limited region of the Galaxy cannot be translated into general relations valid for the whole disc. A better understanding of the s-process at high metallicity is necessary to fully understand the origin of these variations.

Key words. stars: abundances – Galaxy: abundances – Galaxy: disk – Galaxy: evolution – open clusters and associations: general

1. Introduction

Galactic astronomy is experiencing a golden age thanks to the data collected by the *Gaia* satellite (Bailer-Jones et al. 2018; Lindegren et al. 2018; Gaia Collaboration 2018), complemented by ground-based large spectroscopic surveys, such as APOGEE (Majewski et al. 2017), *Gaia*-ESO (Gilmore et al. 2012), GALAH (De Silva et al. 2015; Bland-Hawthorn et al. 2019) and LAMOST (Deng et al. 2012; Cui et al. 2012). The combination of these data is providing a new multi-dimensional view of the structure of our Galaxy. In this framework, important information is provided by our ability to determine stellar ages for the different Galactic populations, which we can use to sketch a Galactic timeline.

Determination of stellar ages is usually based on isochrone fitting: this technique fits a set of isochrones – lines of constant age derived from models – to a set of observed colour-magnitude diagrams. However, during recent decades, several groups have investigated alternative methods to estimate stellar ages, such as for instance the lithium-depletion boundary, asteroseismology, gyrochronology, stellar activity (see Soderblom 2010; Soderblom et al. 2014, for a review on the argument), and chemical clocks (see, e.g. Masseron & Gilmore 2015; Feltzing et al. 2017; Spina et al. 2018; Casali et al. 2019; Delgado Mena et al. 2019, among many papers). In particular, chemical clocks are abundance ratios that show a clear and possibly linear relation with stellar age (in their linear or logarithmic form). The idea is that these ratios, whose relation with stellar age has been calibrated with targets of which the age has been accurately measured (e.g. star clusters, solar twins, asteroseismic targets), allow

us to derive the ages of large sample of stars through empirical relations. Chemical clocks belong to two different broad families: those based on the ratio between elements produced by different stellar progenitors, and thus with different timescales; and those based on the ratio between elements modified by stellar evolution, the alteration of which is strongly dependent on stellar mass.

The former, on which this work focuses, are based on pairs of elements produced with a different contribution of Type II (SNe II) and Type Ia (SNe Ia) supernovae or asymptotic giant branch (AGB) stars. One of the first studies exploring the relation between chemical abundances and stellar age was da Silva et al. (2012). More recently, Nissen (2015) and Spina et al. (2016) found that ratios of [Y/Mg] and [Y/Al] are potentially good age indicators in the case of solar twin stars (solar-like stars in the metallicity range of −0.1 to 0.1 dex); these were also used in other studies such as Nissen et al. (2017), Spina et al. (2018) and Delgado Mena et al. (2019). However, Feltzing et al. (2017) and Delgado Mena et al. (2019) showed that when stars of different metallicities are included, these correlations might not be valid anywhere. There are also some studies on chemical clocks (e.g. [Y/Mg], [Ba/Mg]) in nearby dwarf galaxies, such as that by Skúladóttir et al. (2019).

High-resolution stellar spectra are necessary to determine accurate stellar parameters and abundances, from which we can obtain both stellar ages and abundance ratios. However, standard spectroscopy can suffer from systematic errors, for instance in the model atmospheres and modelling of stellar spectra (Asplund 2005), because of the usual assumptions that affect stars with different stellar parameters and metallicity in different ways, such as for example static and homogeneous one-dimensional models. To minimise the effects of systematic errors when studying solar-like stars, we can perform a differential analysis of those stars relative to the Sun (e.g. Meléndez et al. 2006; Meléndez & Ramírez 2007). Their well-known stellar parameters are extremely important for the calibration of fundamental observable quantities and stellar ages.

Recent studies on solar twins have reached very high precision on stellar parameters and chemical abundances of the order of 0.01 dex in Fe and 0.5 Gyr in age (e.g. Meléndez et al. 2009, 2014; Ramírez et al. 2009, 2014a,b; Liu et al. 2016; Spina et al. 2016, 2018), thanks to the differential analysis technique. This level of precision can be useful for revealing detailed trends in the abundance ratios and opens the door to a more accurate understanding of the Galactic chemical evolution, unveiling more details with respect to the large surveys.

The aim of the present paper is to study the [X/Fe] versus age relations. In Sect. 2, we present our data sets and describe our spectral analysis. In Sect. 3, we discuss the age–[X/Fe] relations. In Sect. 4, we present the relations between stellar ages and chemical clocks. In Sect. 5, we investigate the non-universality of the relations involving s-process elements by comparing with open clusters. In Sect. 6, we discuss the non-universality of the relations between age and chemical abundances involving an s-process element. The application of the relations to the field stars of *Gaia*-ESO high-resolution samples is analysed in Sect. 7. Finally, in Sect. 8, we summarise our results and give our conclusions.

2. Spectral analysis

2.1. Data sample and data reduction

In our analysis we employ stellar spectra collected by the HARPS spectrograph (Mayor et al. 2003). The instrument is installed on the 3.6 m telescope at the La Silla Observatory (Chile) and delivers a resolving power, R, of 115 000 over a 383–690 nm wavelength range.

We obtain the reduced HARPS spectra from the ESO Archive. These are exposures of solar-like stars, with $T_{\rm eff}$ within ±200 K and log g within ±0.2 dex from the solar parameters. In addition, for the analysis we select only spectra with signal-to-noise ratios $S/N > 30\,{\rm px}^{-1}$, which have been acquired with a mean seeing of 0.98″. This sample comprises 28 985 HARPS spectra of 560 stars. In Table 1, we list the dataset IDs, dates of observation, program IDs, seeing, exposure times, S/N and the object names of the single spectra employed in the analysis.

All spectra are normalised using `IRAF`[1]'s `continuum` and are Doppler-shifted with `dopcor` using the stellar radial velocity value determined by the pipeline of the spectrograph. All the exposures of a single object are stacked into a single spectrum using a Python script that computes the medians of the pixels after having re-binned each spectrum to common wavelengths and applied a 3-σ clipping to the pixel values.

In addition to the solar-like stars, the sample includes a solar spectrum acquired with the HARPS spectrograph through observations of the asteroid Vesta to perform a differential analysis with respect to the Sun.

2.2. Stellar parameters and chemical abundances

Equivalent widths (EWs) of the atomic transitions of 25 elements (i.e. C, Na, Mg, Al, Si, S, Ca, Sc, Ti, V, Cr, Mn, Fe, Co, Ni, Cu, Zn, Sr, Y, Zr, Ba, Ce, Nd, Sm, and Eu) reported in Meléndez et al. (2014) and also employed in Spina et al. (2018) and Bedell et al. (2018)[2] are measured with `Stellar diff`[2]. We use the master list of atomic transitions of Meléndez et al. (2014) that includes 98 lines of Fe I, 17 of Fe II, and 183 for the other elements, detectable in the HARPS spectral range (3780–6910 Å).

This code allows the user to interactively select one or more spectral windows for the continuum setting around each line of interest. Ideally, these windows coincide with regions devoid of other absorption lines. Once the continuum is set, we employ the same window settings to calculate continuum levels and fit the lines of interest with Gaussian profiles in every stacked spectrum. Therefore, the same assumption is taken in the choice of the local continuum around a single line of interest for all the spectra analysed here. This is expected to minimise the effects of an imperfect spectral normalisation or unresolved features in the continuum that can lead to larger errors in the differential abundances (Bedell et al. 2014). Furthermore, `Stellar diff` is able to identify points affected by hot pixels or cosmic rays and remove them from the calculation of the continuum. The code delivers the EW of each line of interest along with its uncertainty. The same method for the EW measurement was employed in the high-precision spectroscopic analysis of twin stars by Nagar et al. (2020).

We apply a line clipping, removing 19 lines of Fe I with uncertainties on EWs lying out of the 95% of their probability distribution for more than five stars. These are removed for all of stars from the master line list to calculate their atmospheric parameters ($T_{\rm eff}$, log g, [Fe/H], ξ). The EW measurements are

---

[1] http://ast.noao.edu/data/software
[2] `Stellar diff` is Python code publicly available at https://github.com/andycasey/stellardiff

Table 1. Information about the HARPS spectra of the sample of solar-like stars.

Name	Spectrum ID	Observation date	Program ID	Seeing	Exposure time (s)	S/N
HD 114853	HARPS.2017-03-12T04:22:10.194.fits	12/03/2017	198.C-0836(A)	0.70	900	271
HD 114853	HARPS.2017-07-11T23:49:19.456.fits	11/07/2017	198.C-0836(A)	1.32	900	285
HD 11505	HARPS.2011-09-27T06:37:22.718.fits	27/09/2011	183.C-0972(A)	0.96	900	279
HD 11505	HARPS.2011-09-16T07:05:21.491.fits	16/09/2011	183.C-0972(A)	0.89	900	219
HD 11505	HARPS.2007-10-14T04:10:42.910.fits	14/10/2007	072.C-0488(E)	0.93	900	281
HD 115231	HARPS.2005-05-12T02:34:31.050.fits	12/05/2005	075.C-0332(A)	0.49	900	193
HD 115231	HARPS.2005-05-13T02:40:27.841.fits	13/05/2005	075.C-0332(A)	0.99	900	171
…	…	…	…	…	…	…

Notes. The full version of this table is available at the CDS.

processed by the qoyllur-quipu (q2) code[3] (Ramírez et al. 2014b) which determines the stellar parameters through a line-by-line differential analysis of the EWs of the iron lines relative to those measured in the solar spectrum. Specifically, the q2 code iteratively searches for the three equilibria (excitation, ionisation, and the trend between the iron abundances and the reduced equivalent width log[EW/λ]). The iterations are executed with a series of steps starting from a set of initial parameters (i.e. the nominal solar parameters) and arriving at the final set of parameters that simultaneously fulfil the equilibria. We employ the Kurucz (ATLAS9) grid of model atmospheres (Castelli & Kurucz 2004), the version of MOOG 2014 (Sneden 1973), and we assume the following solar parameters: $T_{\rm eff}$ = 5771 K, log g = 4.44 dex, [Fe/H] = 0.00 dex and ξ = 1.00 km s^{-1} (Ayres et al. 2006). The errors associated with the stellar parameters are evaluated by the code following the procedure described in Epstein et al. (2010) and Bensby et al. (2014). Since each stellar parameter is dependent on the others in the fulfilment of the three equilibrium conditions, the propagation of the error also takes into account this relation between the parameters. The typical precision for each parameter, which is the average of the distribution of the errors, is $\sigma(T_{\rm eff})$ = 10 K, $\sigma(\log g)$ = 0.03 dex, $\sigma([\rm Fe/H])$ = 0.01 dex, and $\sigma(\xi)$ = 0.02 km s^{-1}.

This high precision is related to different factors: (i) the high S/N for a good continuum setting of each spectrum, with a typical value of 800 measured on the 65th spectral order (we calculate the S/N for each combined spectrum as the sum in quadrature of the subexposures); (ii) the high spectral resolution of HARPS spectrograph ($R \sim 115\,000$) which allows blended lines to be resolved; (iii) the differential line-by-line spectroscopic analysis, which allows us to subtract the dependence on log gf and to reduce the systematic errors due to the atmospheric models, comparing stars very similar to the Sun; and (iv) the negligible contribution from telluric lines, since the spectra are the median of several exposures, where the typical number is 50.

Once the stellar parameters and the relative uncertainties are determined for each star, q2 employs the appropriate atmospheric model for the calculation of the chemical abundances. All the elemental abundances are scaled relative to the values obtained for the Sun on a line-by-line basis. In addition, through the `blends` driver in the MOOG code and adopting the line list from the Kurucz database, q2 is able to take into account the hyperfine splitting effects in the abundance calculations of Y, Ba, and Eu (we assumed the HFS line list adopted by Meléndez et al.

2014). We note that lines for some elements suffer from HFS; in the analysis presented here, the EWs are measured for these lines and MOOG is used to calculate the EWs taking the HFS into account (as described above). Although this is correct in principle, it does leave the analysis open to some possible errors. Ideally, the lines should be fully modelled and the observed line shape compared with the modelled one (see e.g. Bensby et al. 2005; Feltzing et al. 2007). However, the analysis presented here is robust enough for our purposes, because we deal with stars that have very similar stellar parameters ($T_{\rm eff}$ and log g close to solar ones). This means that any systematic error should cancel to first order in the analysis. Finally, the q2 code determines the error budget associated with the abundances [X/H] by summing in quadrature the observational error due to the line-to-line scatter from the EW measurements (standard error), and the errors in the atmospheric parameters. When only one line is detected, as is the case for Sr and Eu, the observational error is estimated through the uncertainty on the EW measured by `Stellar diff`. The final stellar parameters and chemical abundances are listed in Tables 2 and 3, respectively.

2.3. Stellar ages

During their lives, stars evolve along a well-defined stellar evolutionary track in the Hertzsprung-Russell diagram that mainly depends on their stellar mass and metallicity. Therefore, if the stellar parameters are known with sufficient precision, it is possible to estimate the age by comparing the observed properties with the corresponding model. Following this approach, we estimate the stellar ages using the q2 code, which also computes a probability distribution function for age for each star of our sample. It makes use of a grid of isochrones to perform an isochrone fitting comparing the stellar parameters with the grid results and taking into account the uncertainties on the stellar parameters. The q2 code uses the difference between the observed parameters and the corresponding values in the model grid as weight to calculate the probability distribution; it performs a maximum-likelihood calculation to determine the most probable age (i.e. the peak of the probability distribution). The q2 code also calculates the 68% and 95% confidence intervals, and the mean and standard deviation of these values. We adopt the grid of isochrones computed with the Yale-Potsdam Stellar Isochrones (YaPSI) models (Spada et al. 2017). We take into account the α-enhancement effects on the model atmospheres, using the relation [M/H] = [Fe/H] + log($0.638 \times 10^{[\alpha/{\rm Fe}]} + 0.362$) (Salaris et al. 1993), where we employ magnesium as a proxy for the α-abundances. Typical uncertainties on our age determinations (i.e. the average of the half widths of the 68% confidence

---

[3] The q2 code is a free Python package, available at `https://github.com/astroChasqui/q2`

Table 2. Atmospheric parameters and stellar ages determined for the sample of solar-like stars.

Id	RA (J2000)	Dec	$T_{\rm eff}$ (K)	$\log g$ (dex)	[Fe/H] (dex)	ξ (km s^{-1})	Age (Gyr)
HD 220507	23:24:42.12	−52:42:06.76	5689 ± 3	4.26 ± 0.01	0.019 ± 0.003	1.02 ± 0.01	10.7 ± 0.6
HD 207700	21:54:45.20	−73:26:18.55	5671 ± 3	4.28 ± 0.01	0.052 ± 0.003	1.00 ± 0.01	10.3 ± 0.5
HIP 10303	02:12:46.64	−02:23:46.79	5710 ± 3	4.39 ± 0.01	0.096 ± 0.002	0.93 ± 0.01	6.5 ± 0.6
HD 115231	13:15:36.97	+09:00:57.71	5683 ± 5	4.35 ± 0.01	−0.098 ± 0.003	0.97 ± 0.01	10.7 ± 0.6
HIP 65708	13:28:18.71	−00:50:24.70	5761 ± 5	4.26 ± 0.01	−0.047 ± 0.004	1.12 ± 0.01	9.9 ± 0.5
HD 184768	19:36:00.65	+00:05:28.27	5687 ± 4	4.31 ± 0.01	−0.055 ± 0.003	1.02 ± 0.01	11.0 ± 0.5
HIP 117367	23:47:52.41	+04:10:31.72	5866 ± 3	4.36 ± 0.01	0.024 ± 0.003	1.14 ± 0.01	5.6 ± 0.5
…	…	…	…	…	…	…	…

Notes. The full version of this table is available at the CDS.

Table 3. Chemical abundances for the sample of solar-like stars.

Id	[CI/H]	[NaI/H]	[MgI/H]	[AlI/H]	[SiI/H]	[SI/H]	[CaI/H]	[ScI/H]	[ScII/H]
HD 220507	0.145 ± 0.021	0.062 ± 0.007	0.161 ± 0.015	0.175 ± 0.007	0.085 ± 0.002	0.084 ± 0.015	0.070 ± 0.004	0.092 ± 0.023	0.126 ± 0.011
HD 207700	0.171 ± 0.012	0.094 ± 0.008	0.169 ± 0.014	0.208 ± 0.010	0.115 ± 0.003	0.120 ± 0.006	0.099 ± 0.004	0.129 ± 0.027	0.157 ± 0.01
HIP 10303	0.087 ± 0.007	0.106 ± 0.002	0.093 ± 0.009	0.123 ± 0.006	0.101 ± 0.001	0.075 ± 0.032	0.099 ± 0.004	0.098 ± 0.015	0.121 ± 0.008
HD 115231	−0.038 ± 0.011	−0.143 ± 0.003	0.044 ± 0.038	0.02 ± 0.017	−0.047 ± 0.003	−0.061 ± 0.007	−0.019 ± 0.005	−0.012 ± 0.031	−0.011 ± 0.006
HIP 65708	0.077 ± 0.019	−0.026 ± 0.021	0.053 ± 0.007	0.074 ± 0.003	0.003 ± 0.003	−0.008 ± 0.012	−0.003 ± 0.006	0.013 ± 0.017	0.043 ± 0.013
HD 184768	0.098 ± 0.155	−0.007 ± 0.002	0.074 ± 0.013	0.13 ± 0.002	0.031 ± 0.002	0.040 ± 0.019	0.005 ± 0.005	0.049 ± 0.027	0.091 ± 0.005
HIP 117367	0.003 ± 0.082	0.076 ± 0.012	0.040 ± 0.006	0.052 ± 0.005	0.047 ± 0.002	0.031 ± 0.013	0.021 ± 0.004	0.033 ± 0.007	0.056 ± 0.006
…	…	…	…	…	…	…	…	…	…

[TiI/H]	[TiII/H]	[VI/H]	[CrI/H]	[CrII/H]	[MnI/H]	[FeI/H]	[FeII/H]	[CoI/H]	[NiI/H]
0.124 ± 0.005	0.127 ± 0.006	0.089 ± 0.006	0.032 ± 0.006	0.025 ± 0.009	−0.005 ± 0.009	0.019 ± 0.003	0.016 ± 0.005	0.084 ± 0.004	0.030 ± 0.003
0.160 ± 0.005	0.148 ± 0.007	0.137 ± 0.007	0.070 ± 0.006	0.057 ± 0.010	0.066 ± 0.006	0.052 ± 0.003	0.050 ± 0.005	0.145 ± 0.003	0.076 ± 0.003
0.112 ± 0.004	0.108 ± 0.006	0.121 ± 0.006	0.110 ± 0.005	0.108 ± 0.007	0.159 ± 0.008	0.096 ± 0.003	0.100 ± 0.005	0.119 ± 0.004	0.113 ± 0.004
0.025 ± 0.006	0.003 ± 0.007	−0.035 ± 0.006	−0.087 ± 0.006	−0.101 ± 0.006	−0.207 ± 0.010	−0.097 ± 0.004	−0.101 ± 0.007	−0.084 ± 0.009	−0.123 ± 0.004
0.048 ± 0.006	0.057 ± 0.007	0.003 ± 0.006	−0.051 ± 0.006	−0.042 ± 0.005	−0.140 ± 0.007	−0.047 ± 0.005	−0.047 ± 0.006	−0.020 ± 0.007	−0.058 ± 0.004
0.076 ± 0.005	0.066 ± 0.006	0.042 ± 0.009	−0.050 ± 0.005	−0.05 ± 0.008	−0.101 ± 0.009	−0.055 ± 0.004	−0.055 ± 0.006	0.043 ± 0.004	−0.029 ± 0.004
0.030 ± 0.005	0.039 ± 0.005	0.029 ± 0.005	0.020 ± 0.004	0.031 ± 0.007	0.013 ± 0.006	0.025 ± 0.003	0.021 ± 0.005	0.042 ± 0.007	0.035 ± 0.003
…	…	…	…	…	…	…	…	…	…

[CuI/H]	[ZnI/H]	[SrI/H]	[YII/H]	[ZrII/H]	[BaII/H]	[CeII/H]	[NdII/H]	[SmII/H]	[EuII/H]
0.103 ± 0.036	0.138 ± 0.022	−0.013 ± 0.007	−0.036 ± 0.01	−0.044 ± 0.02	−0.028 ± 0.005	0.041 ± 0.017		0.065 ± 0.011	0.103 ± 0.007
0.145 ± 0.034	0.180 ± 0.024	0.001 ± 0.006	−0.014 ± 0.007	−0.038 ± 0.023	0.002 ± 0.008	0.074 ± 0.016	0.064 ± 0.010	0.065 ± 0.008	0.126 ± 0.007
0.128 ± 0.008	0.097 ± 0.010	0.158 ± 0.006	0.135 ± 0.007	0.103 ± 0.023	0.077 ± 0.013	0.083 ± 0.025	0.111 ± 0.010		0.081 ± 0.008
−0.116 ± 0.010	−0.083 ± 0.004	−0.097 ± 0.007	−0.102 ± 0.017	−0.066 ± 0.008	−0.076 ± 0.012	0.039 ± 0.014	0.100 ± 0.008	0.159 ± 0.007	0.17 ± 0.008
−0.027 ± 0.020	0.027 ± 0.009	−0.101 ± 0.008	−0.095 ± 0.007	−0.091 ± 0.009	−0.072 ± 0.014	0.016 ± 0.016	0.059 ± 0.007	0.097 ± 0.008	0.057 ± 0.008
0.024 ± 0.025	0.081 ± 0.022	−0.068 ± 0.006	−0.114 ± 0.007	−0.119 ± 0.005	−0.107 ± 0.005	−0.009 ± 0.014		0.004 ± 0.012	0.041 ± 0.008
0.043 ± 0.021	0.037 ± 0.008	0.007 ± 0.005	0.004 ± 0.008	−0.015 ± 0.005	−0.012 ± 0.006	0.014 ± 0.017	0.043 ± 0.010	0.002 ± 0.010	0.026 ± 0.008
…	…	…	…	…	…	…	…	…	…

Notes. The full version of this table is available at the CDS.

intervals) are 0.9 Gyr. The ages of the solar-like stars can be found in Table 2.

2.4. A check on the spectroscopic log g

In Fig. 1, we present a comparison between the log g values derived through our spectroscopic analysis and those from *Gaia* photometry and parallaxes. Photometric gravities were obtained using the following equation

$$\log(g) = \log(M/M_\odot) + 0.4 \times M_{\rm bol} + 4 \times \log(T_{\rm eff}) - 12.505 \quad (1)$$

where $M/M_\odot$ is the stellar mass (in solar mass units) computed through a maximum-likelihood calculation performed by q2 as described in the previous section, $M_{\rm bol}$ is the bolometric magnitude obtained from the luminosity published in the *Gaia* DR2 catalogue (Lindegren et al. 2018) using the relation $M_{\rm bol} = 4.75 - 2.5 \times \log(L/L_\odot)$, and $T_{\rm eff}$ is the spectroscopic effective temperature (we tested the use of the *Gaia* photometric $T_{\rm eff}$ and the variations in log g are negligible). In Fig. 1, we plot

solar-like stars with relative errors on their parallaxes lower than 10% and with uncertainties on their stellar parameters within 90% of their distributions. Photometric surface gravities derived via stellar distances agree fairly well with the spectroscopic gravities suggesting that 3D non local thermodynamic equilibrium (non-LTE) effects on the Fe I and Fe II abundances have only a small effect on the derived spectroscopic gravities. The median of the difference between the two log g is ~0.02 dex, which is smaller than the scatter due to their uncertainties of the order of ~0.03 dex. Figure 1 shows that the consistency level of the two sets of gravities depends on stellar metallicity. Namely, metal-rich stars have spectroscopic gravities that are slightly smaller than the photometric values, while those obtained for the metal-poor stars are higher. The slight discrepancy between the two gravities could be imputed to a number of factors, including systematic effects in the differential analysis of stars with metal-licities that are different from that of the Sun, the dependence of the grid of isochrones on stellar metallicity, or other assumptions on the photometric log g calculation.
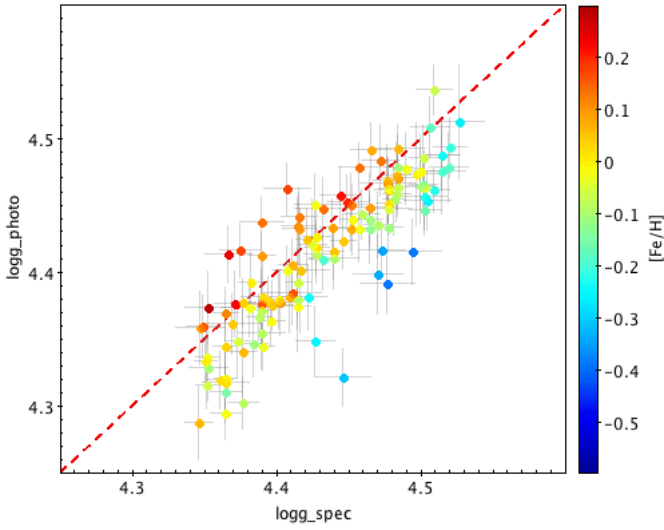
Fig. 1. Comparison between photometric and spectroscopic log g, where the stars are colour-coded by metallicity.
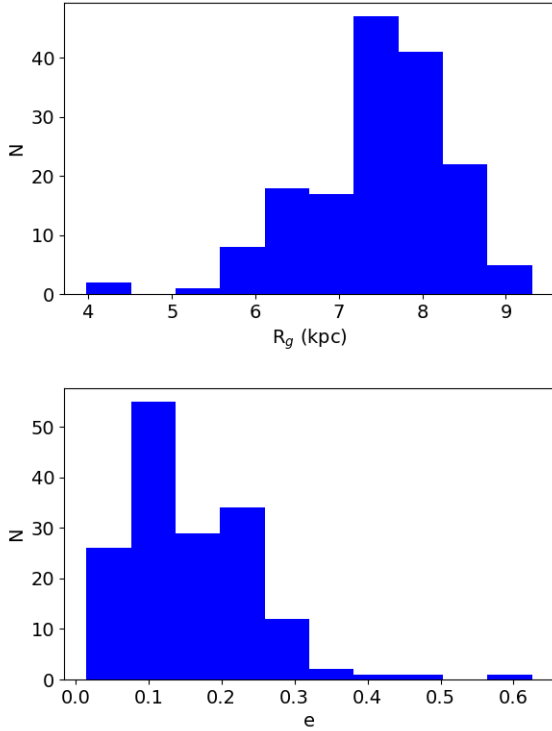
Fig. 2. Distribution of the guiding radius R_g (*top panel*) and a distribution of the eccentricity e (*bottom panel*) for our sample of solar-like stars.

2.5. Orbital parameters

All stars in our sample are observed by the *Gaia* satellite, and they are available in the DR2 database. We use the `GalPy`[4] package of Python, in which the model `MWpotential2014` for the gravitational potential of the Milky Way is assumed (Bovy 2015). Through `AstroPy` and the astrometric information by *Gaia* DR2, we convert the celestial coordinates into the Galactocentric radius (R_GC) and height above the Galactic plane (z), assuming a solar Galactocentric distance $R_0 = 8$ kpc and a

---

[4] Code available at http://github.com/jobovy/galpy

---

height above the Plane $z_0 = 0.025$ kpc (Jurić et al. 2008). A circular velocity at the solar Galactocentric distance equal to $V_c = 220$ km s^{-1} and the Sun's motion with respect to the local standard of rest $[U_\odot, V_\odot, W_\odot] = [11.1, 12.24, 7.25]$ km s^{-1} (Schönrich et al. 2010) are used to calculate the Galactic space velocity (U, V, W) of each star. As results of the orbit computation, we obtain, among several parameters, the eccentricity of the orbit e, the perigalacticon and apogalacticon radii, and the guiding radius R_g.

In Fig. 2 we present two different panels showing the distribution of guiding radius R_g and eccentricity e. Approximately 95% of the stars in our sample have R_g between 6 and 9 kpc (top panel) and orbits with $e < 0.3$ (bottom panel). Only two stars have a guiding radius of ~4–4.5 kpc and very eccentric orbits ($e \sim 0.6$), implying their birth place is located far from the solar neighbourhood. If we assume that the R_g is a good proxy of the Galactocentric distance where the stars were formed, then we can conclude that the stars in our sample were born within a restricted range of Galactocentric distances compared to the typical variation of the [X/Fe] ratios with R_g predicted by models (e.g. Magrini et al. 2009, 2017). However, it is possible that a fraction of the stars in our sample have not preserved their kinematical properties due to interaction with spiral arms or giant molecular clouds losing all information on their origin, and therefore we cannot exclude the presence of other migrators in our sample.

3. [X/Fe] versus age relations

In this section, we briefly reiterate the main sites of production of the chemical elements and how they affect the [X/Fe]–age relation.

In Fig. 3, we show abundance ratios versus age trends for 24 elements and/or ions over iron in the metallicity range -0.1 to $+0.1$ dex. We select stars in $T_{\mathrm{eff},\odot} \pm 200$ K and log $g_\odot \pm 0.2$ dex, removing those with larger uncertainties on the atmospheric parameters, that is larger than 95% of their distributions. The stars are plotted with different symbols and colours: the red diamonds are thick-disc stars, whereas the thin-disc stars are shown with blue circles. We select the thick-disc stars through the [α/Fe] versus [Fe/H] plane with [α/Fe] = ([Ca/Fe]+[Si/Fe]+[Ti/Fe]+[Mg/Fe])/4 (excluding S because of its large scatter). The separation in chemical properties is also related to the age separation between the two populations, which is located at a look-back time of ~8 Gyr (Haywood et al. 2013; Nissen 2015; Bensby et al. 2014). The different slopes for the relations of these elements versus age outline a different contribution of the main stellar nucleosynthesis processes, such as for instance, those related to the ejecta of SNe II, SNe Ia, and AGB stars. As we can see from Fig. 3, the relations of [α/Fe] (with α elements of our sample Mg, Si, S, Ca, Ti) versus age have positive slopes, in agreement with their production over a shorter timescale with respect to iron. SNe II indeed eject mainly α-elements and elements up to the iron peak, including Fe, into the interstellar medium (ISM) within short timescales ($<10^{-2}$ Gyr); while SNe Ia produce mainly Fe and iron-peak elements (e.g. Cr, Mn, Co, Ni), with a minor amount of α-elements and over longer timescales (~1 Gyr; Matteucci 2014; Spina et al. 2016). Indeed, at the beginning of the Galactic formation, the metal content of the most metal-poor stars was produced by SNe II. At later times, SNe Ia started to explode, contributing to a metal mixture with a smaller [α/Fe] ratio with respect to the oldest stars and creating the typical positive slope for [α/Fe] versus age trends. Therefore, the iron peak
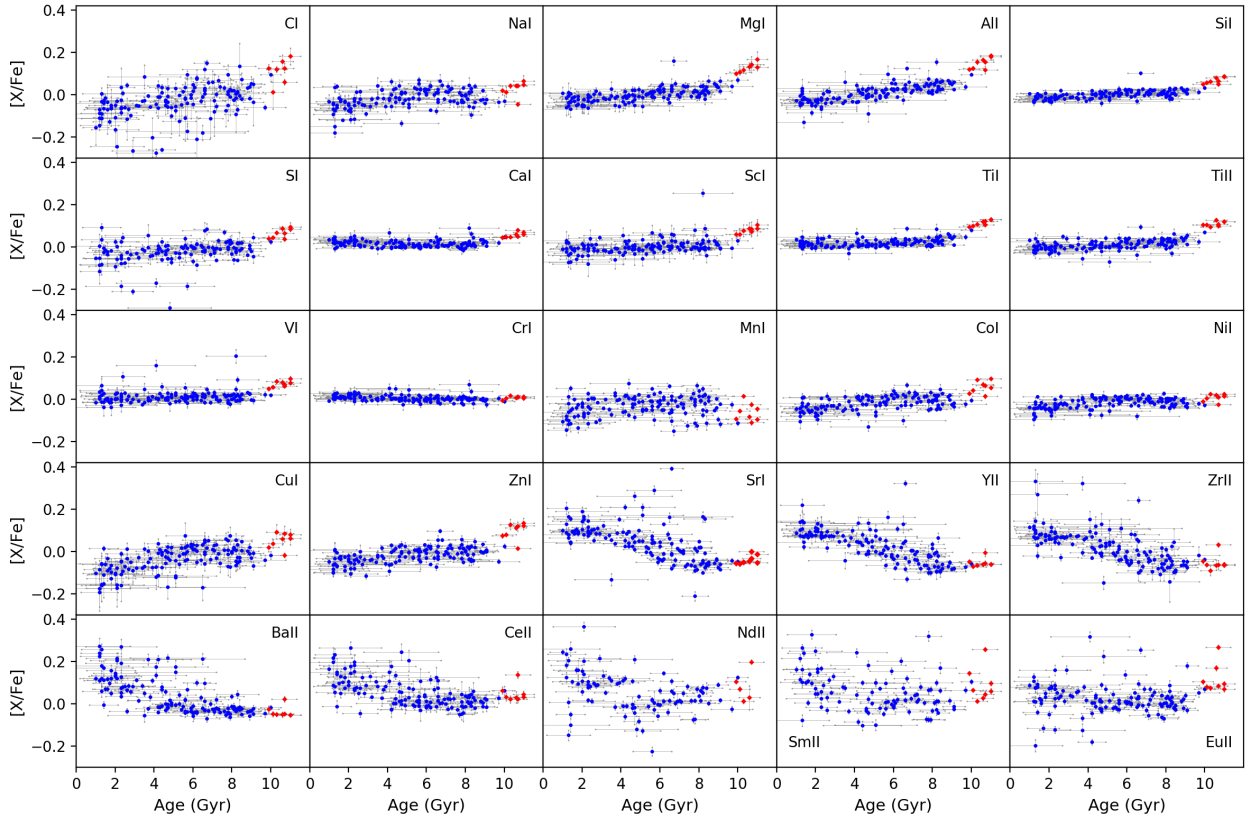
Fig. 3. [X/Fe] ratio as a function of stellar age. The blue dots represent the thin disc stars, while the red diamonds are the thick disc populations. The stars are within the metallicity range of $-0.1 < $ [Fe/H] $ < +0.1$ dex.

elements (V, Cr, Mn, Co, Ni, Cu, Zn) over iron show slightly positive or negligible slopes with age. This is consistent, within the errors, with a null slope that reflects similar mechanisms of production of all iron-peak elements and Fe. Finally, neutron capture elements are produced in the ejecta of AGB stars (mainly *s*-elements) or during mergers of neutron stars or a neutron star and a black hole (mainly r-elements). Indeed, almost pure *s*-process elements (e.g. Sm, Sr, Zr, Y) over iron have a negative slope due to their delayed production from successive captures of neutrons by iron-peak elements in low-mass AGB stars with respect to the early contribution of SNe Ia and SNe II that produce iron. The elements with a lower contribution from the *s*-process and a high contribution from the *r*-process, such as Eu (see Fig. 6 in Spina et al. 2018), have flatter [X/Fe]–age distributions than the almost pure *s*-process elements. This means that the production of *s*-process elements has been more efficient within the last gigayear.

4. Chemical clocks

Abundance ratios of pairs of elements produced over different timescales (e.g. [Y/Mg] or [Y/Al]) can be used as valuable indicators of stellar age. Their [X/Fe] ratios show opposite behaviours with respect to stellar age (see e.g. [Mg/Fe] and [Y/Fe] in Fig. 3, decreasing and increasing, respectively, with stellar age). Therefore, their ratio, for example [Y/Mg], shows a steep increasing trend with stellar age. However, as pointed out by Feltzing et al. (2017) and Delgado Mena et al. (2019), their relations might have a secondary dependence on metallicity. Moreover, Titarenko et al. (2019) found the existence of different

relations between ages and [Y/Mg] for a sample of stars belonging to the thin and thick discs.

The most studied chemical clocks in the literature are [Y/Mg] and [Y/Al] (Tucci Maia et al. 2016; Nissen 2015; Nissen et al. 2017; Slumstrup et al. 2017; Spina et al. 2016, 2018). However, some recent studies have extended the list of chemical clocks to other ratios and found interesting results (Delgado Mena et al. 2019; Jofré et al. 2020).

4.1. Simple linear regression

In Fig. 4, we show the effect of metallicity in our sample stars, where two chemical clocks ([Y/Mg] and [Y/Al]) are plotted as a function of stellar age. The points are colour-coded by metallicity and the linear fits in four different metallicity bins ([Fe/H] < -0.3, $-0.3 < $ [Fe/H] < -0.1, $-0.1 < $ [Fe/H] $< +0.1$, and [Fe/H] $> +0.1$) are shown. The slopes of these fits depend on the metal content: the more metal-rich sample has a flatter slope, while the more metal-poor samples have steeper slopes.

In Table 4, we show the parameters of orthogonal distance regression fits for [Y/Mg] and [Y/Al]. In the first three metallicity bins for both abundance ratios, the difference in slopes is within 1-σ, not showing a strong variation with metallicity in the subsolar and solar ranges. On the other hand, in the more metal-rich bin, the slope is definitively flatter. The slopes obtained in the solar metallicity bin ($-0.1 < $ [Fe/H] $< +0.1$) are in good agreement with previous literature results (Delgado Mena et al. 2019; Spina et al. 2018) for the same metallicity range. The differences in the slopes and intercepts obtained in the high-metallicity bin are statistically significant (see the Pearson correlation coefficient in Table 4). This indicates that the
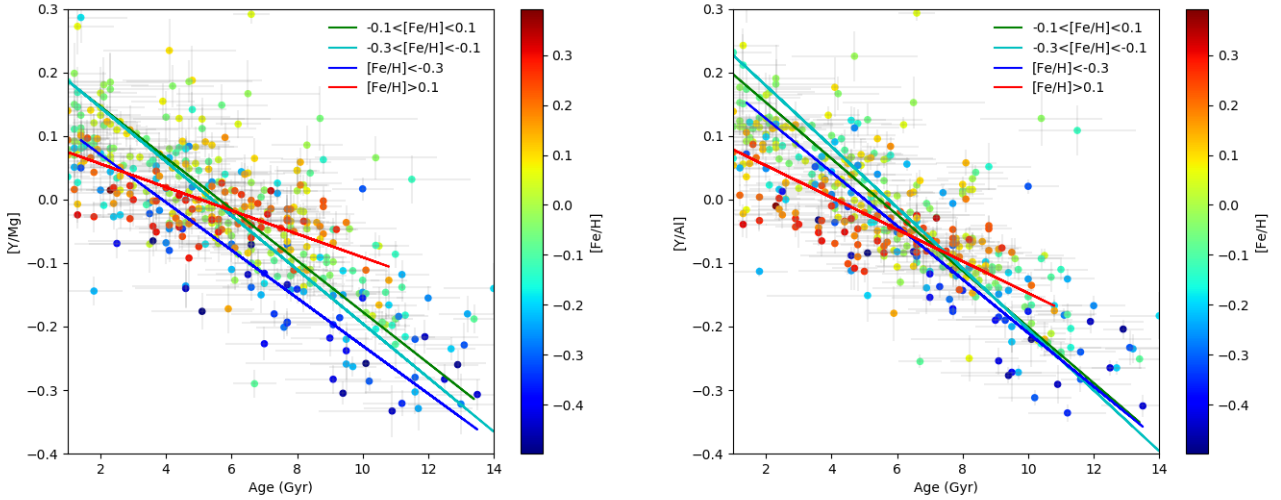
Fig. 4. [Y/Mg] and [Y/Al] as a function of age. The dots are colour-coded by [Fe/H]. The lines correspond to the linear functions described in Table 4 in four different bins of metallicity: [Fe/H] < −0.3 (blue), −0.3 < [Fe/H] < −0.1 (turquoise), −0.1 < [Fe/H] < +0.1 (green), and [Fe/H] > +0.1 (red).

Table 4. Slopes and intercepts of the four linear fits shown in Fig. 4.

[A/B]	Metallicity bin	Slope	Intercept	Pearson coefficient
[Y/Mg]	[Fe/H] < −0.3	−0.038 ± 0.005	0.146 ± 0.050	−0.76
[Y/Mg]	−0.3 < [Fe/H] < −0.1	−0.042 ± 0.004	0.223 ± 0.029	−0.63
[Y/Mg]	−0.1 < [Fe/H] < +0.1	−0.040 ± 0.002	0.228 ± 0.015	−0.74
[Y/Mg]	[Fe/H] > +0.1	−0.018 ± 0.002	0.093 ± 0.010	−0.59
[Y/Al]	[Fe/H] < −0.3	−0.042 ± 0.005	0.212 ± 0.035	−0.83
[Y/Al]	−0.3 < [Fe/H] < −0.1	−0.048 ± 0.004	0.275 ± 0.031	−0.64
[Y/Al]	−0.1 < [Fe/H] < +0.1	−0.044 ± 0.002	0.241 ± 0.015	−0.79
[Y/Al]	[Fe/H] > +0.1	−0.025 ± 0.002	0.104 ± 0.012	−0.64

metallicity is an important additional parameter that cannot be neglected in the use of abundance ratios to derive stellar ages.

Following the work of Delgado Mena et al. (2019), we analyse the correlation coefficients between abundance ratios and stellar age for other ratios in addition to [Y/Al] and [Y/Mg]. We consider ratios between s-process (negative slope of [X/Fe] vs. age) and α-elements (positive slope) or iron-peak elements (flat/slightly positive slope). We evaluate the correlation between chemical clocks and stellar age using the Pearson coefficient. In Table 5, we show the abundances ratios with the highest Pearson correlation coefficient for the chemical abundance ratios studied in this work.

4.2. Multivariate linear regression

As shown in Fig. 4, the metallicity represents a third important variable to take into account when we search for the relations between abundance ratios and stellar age. Our sample, which is composed of stars similar to the Sun, is indeed a good way to test the metallicity dependence in a range from −0.7 to +0.4 dex, disentangling the effect of the other parameters.

In our analysis, we consider age (measured from the isochrone fitting via maximum-likelihood calculation) and metallicity (via spectroscopic analysis) as independent variables, while the abundance ratios are the dependent variables. We derive the relations in the form [A/B] = f(X), where X represents the independent variables, in this case age and [Fe/H], while

Table 5. Pearson coefficients of [A/B] abundance ratios vs. stellar age.

[A/B]	Pearson coefficient
[Y/Mg]	−0.87
[Y/Al]	−0.88
[Y/Ca]	−0.87
[Y/Si]	−0.86
[Y/TiI]	−0.87
[Y/TiII]	−0.86
[Y/Sc]	−0.84
[Y/V]	−0.84
[Y/Co]	−0.80
[Sr/Mg]	−0.84
[Sr/Al]	−0.87
[Sr/TiI]	−0.83
[Sr/TiII]	−0.81

[A/B] is a generic abundance ratio used as a chemical clock. For each relation, we produce the adjusted R^2 (adj-R^2) parameter, a goodness-of-fit measurement for multivariate linear regression models, taking into account the number of independent variables. We perform the fitting, selecting the *best* sample of solar-like stars: ± 100 K and ± 0.1 dex from the T_{eff} and the log g of the Sun, respectively. Stars with uncertainties on stellar parameters and chemical abundances larger than 95% of their

Table 6. Multivariate linear regression parameters.

[A/B]	c	x_1	x_2	Δc	Δx_1	Δx_2	adj$-R^2$	c'	x'_1	x'_2
[Y/Mg]	0.161	0.155	−0.031	0.009	0.028	0.002	0.80	5.245	5.057	−32.546
[Y/Al]	0.172	0.028	−0.035	0.009	0.029	0.002	0.78	4.954	0.796	−28.877
[Y/TiII]	0.132	0.146	−0.026	0.008	0.026	0.002	0.78	5.026	5.591	−38.219
[Y/TiI]	0.116	0.185	−0.025	0.008	0.024	0.001	0.81	4.597	7.326	−39.514
[Y/Ca]	0.099	0.142	−0.020	0.007	0.020	0.001	0.79	5.000	7.143	−50.462
[Y/Sc]	0.137	0.052	−0.026	0.009	0.029	0.002	0.67	5.304	2.017	−38.649
[Y/Si]	0.135	0.076	−0.025	0.008	0.025	0.001	0.75	5.311	3.003	−39.325
[Y/V]	0.116	−0.020	−0.024	0.008	0.026	0.002	0.66	4.869	−0.852	−41.921
[Y/Co]	0.163	−0.061	−0.029	0.009	0.029	0.002	0.67	5.699	−2.146	−35.018
[Sr/Mg]	0.184	0.218	−0.030	0.010	0.032	0.002	0.77	6.129	7.276	−33.401
[Sr/Al]	0.194	0.089	−0.034	0.010	0.031	0.002	0.77	5.737	2.631	−29.532
[Sr/TiI]	0.139	0.248	−0.025	0.009	0.028	0.002	0.78	5.655	10.103	−40.753
[Sr/TiII]	0.154	0.209	−0.025	0.010	0.031	0.002	0.74	6.052	8.203	−39.268
[Y/Zn]	0.170	−0.075	−0.029	0.009	0.028	0.002	0.68	5.853	−2.595	−34.370
[Sr/Zn]	0.194	−0.006	−0.029	0.010	0.032	0.002	0.65	6.819	−0.220	−35.072
[Sr/Si]	0.159	0.139	−0.025	0.010	0.031	0.002	0.70	6.341	5.553	−39.994
[Zn/Fe]	−0.065	0.061	0.012	0.006	0.019	0.001	0.42	5.481	−5.180	84.381

Notes. Coefficients c, x_1, and x_2 of the relations [A/B] = $c + x_1 \cdot$ [Fe/H] $+ x_2 \cdot$ Age, where [Fe/H] and age are the independent variables. Δc, Δx_1, and Δx_2 are the uncertainties on the coefficients. c', x'_1, and x'_2 are the coefficients of the inverted stellar dating relation Age = $c' + x'_1 \cdot$ [Fe/H] $+ x'_2 \cdot$ [A/B]. Finally, adj$-R^2$ is the adjusted R^2 parameter.

distributions or with uncertainties on age $\gtrsim 50\%$ and stars with an upper limit in age are excluded. These upper limits are due to their probability age distributions, which are truncated before they reach the maximum. This truncation due to the border of the YAPSI isochrone grid excludes solar-like stars younger than 1 Gyr. In addition, we identify and exclude stars that are anomalously rich in at least four *s*-elements in comparison to the bulk of thin disc stars. These are easily identifiable because they lie outside 3-σ from a linear fit of data in Fig. 3: namely CWW097, HIP 64150, HD 140538, HD 28701, HD 49983, HD 6434, and HD 89124. We also exclude a few stars belonging to the halo ($v_{\text{tot}} > 200\,\text{km s}^{-1}$).

The parameters of the multivariate linear regressions are shown in Table 6: the constant $c \pm \Delta c$, the coefficient of [Fe/H] $x_1 \pm \Delta x_1$, and the coefficient of [A/B] $x_2 \pm \Delta x_2$. The regressions with the lower adj-R^2 are those involving abundance ratios between *s*-process and iron-peak elements. These ratios have flatter trends with stellar age. In the following analysis, we consider only the relations with adj$-R^2 > 0.70$.

Finally, we invert the relations [A/B] = f(Age, [Fe/H]) to have relations in the form Age = f([A/B], [Fe/H]), referred to as "stellar dating relations" hereafter. The new coefficients are shown in Table 6, labelled as c', x'_1, and x'_2, the constant and coefficients of [Fe/H] and [A/B], respectively.

First, we validate the multivariate regressions by comparing the ages derived with them and the input values, that is, ages obtained with the isochrone fitting through the maximum-likelihood calculation. The agreement is good and there are no trends.

We then compare our results to those of Delgado Mena et al. (2019) in which a similar approach was used to estimate dating relations between abundance ratios, metallicity, and age. The main differences between our work and that of Delgado Mena et al. (2019) are as follows: (i) the selection of the calibration sample, which is composed of 1111 FGK stars, includes stars with a large variety of stellar parameters and not only solar-like stars, as in ours; (ii) Delgado Mena et al. (2019) do not perform a differential analysis; and (iii) they use a grid of isochrones

based on PARSEC stellar evolutionary models, together with *Gaia* DR2 parallaxes, to determine the stellar ages. To validate our stellar dating relations, we apply both relations to the sample of solar-like stars in common between the present work and Delgado Mena et al. (2019). Despite the differences in the two approaches, the agreement between the ages inferred with our relations and those of Delgado Mena et al. (2019) is good (see Fig. 5, where the red lines are the one-to-one relations). There are no major trends between the two sets of ages.

5. Comparison with open clusters

A meaningful validation of our relations is a comparison with star clusters, which are important benchmarks for stellar age. In this section, we compare the age from the literature for 19 open clusters available in the *Gaia*-ESO survey (GES) iDR5 with the corresponding ages derived using our stellar dating relations.

5.1. The open cluster sample in the Gaia-ESO iDR5

We select open clusters (OCs) available in the *Gaia*-ESO iDR5 survey (GES; Gilmore et al. 2012; Randich et al. 2013). We adopt the cluster membership analysis described in Casali et al. (2019). Briefly, the membership is based on a Bayesian approach, which takes into account both GES and *Gaia* information. Membership probabilities are estimated from the radial velocities (RVs; from GES) and proper motion velocities (from *Gaia*) of stars observed with the GIRAFFE spectrograph, using a maximum likelihood method (see Casali et al. 2019, for more details). For our analysis, we select stars with a minimum membership probability of 80%.

The clusters are listed in Table 7, where we summarise their basic properties from the literature: coordinates, Galactocentric distances (R_{GC}), heights above the plane (z), median metallicity [Fe/H], ages, and the references for ages and distances. We use homogeneous data sets for age from the GES papers mentioned above.
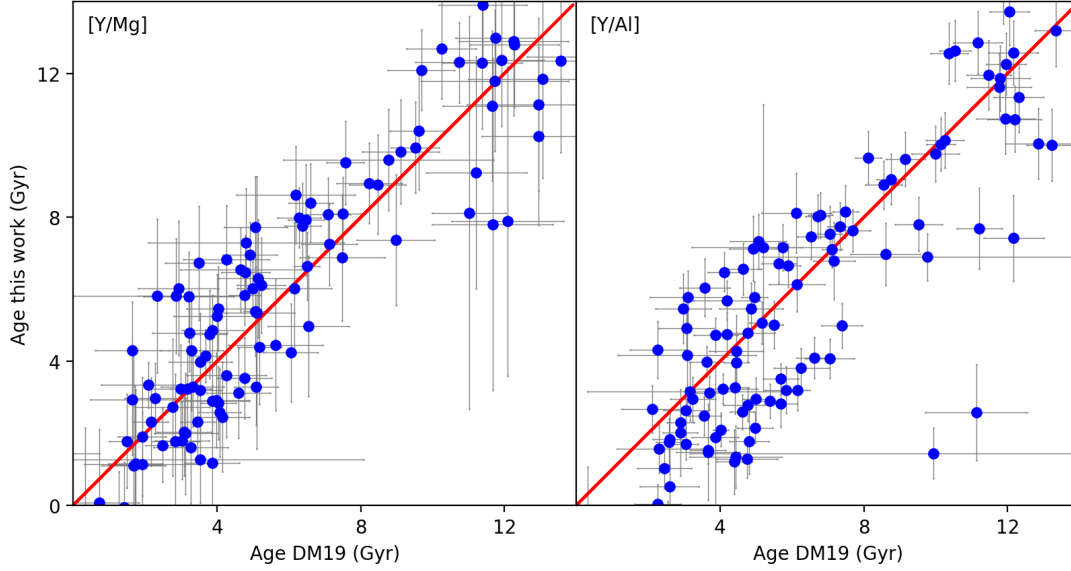
Fig. 5. Comparison of the ages derived by Delgado Mena et al. (2019) and those inferred in the present work with both of our relations: [Y/Mg] and [Y/Al] vs. Age. The circles are the ages of the stars in common between the two works. The red lines are the one-to-one relations.

Table 7. Parameters of the open clusters in the GES sample.

Cluster	RA [a] (J2000)	Dec [a]	R_{GC} (kpc)	z (pc)	[Fe/H] [a] (dex)	Age (Gyr)	Ref. age and distance
NGC 6067	16:13:11	−54:13:06	6.81 ± 0.12	−55 ± 17	0.20 ± 0.08	0.10 ± 0.05	Alonso-Santiago et al. (2017)
NGC 6259	17:00:45	−44:39:18	7.03 ± 0.01	−27 ± 13	0.21 ± 0.04	0.21 ± 0.03	Mermilliod et al. (2001)
NGC 6705	18:51:05	−06:16:12	6.33 ± 0.16	−95 ± 10	0.16 ± 0.04	0.3 ± 0.05	Cantat-Gaudin et al. (2014)
NGC 6633	18:27:15	+06 30 30	7.71		−0.01 ± 0.11	0.52 ± 0.10	Randich et al. (2018)
NGC 4815	12:57:59	−64:57:36	6.94 ± 0.04	−95 ± 6	0.11 ± 0.01	0.57 ± 0.07	Friel et al. (2014)
NGC 6005	15:55:48	−57:26:12	5.97 ± 0.34	−140 ± 30	0.19 ± 0.02	0.7 ± 0.05	Hatzidimitriou et al. (2019)
Trumpler 23	16:00:50	−53:31:23	6.25 ± 0.15	−18 ± 2	0.21 ± 0.04	0.8 ± 0.1	Jacobson et al. (2016)
Melotte 71	07:37:30	−12:04:00	10.50 ± 0.10	+210 ± 20	−0.09 ± 0.03	0.83 ± 0.18	Salaris et al. (2004)
Berkeley 81	19:01:36	−00:31:00	5.49 ± 0.10	−126 ± 7	0.22 ± 0.07	0.86 ± 0.10	Magrini et al. (2015)
NGC 6802	19:30:35	+20:15:42	6.96 ± 0.07	+36 ± 3	0.10 ± 0.02	1.0 ± 0.1	Jacobson et al. (2016)
Rup 134	17:52:43	−29:33:00	4.60 ± 0.10	−100 ± 10	0.26 ± 0.06	1.0 ± 0.2	Carraro et al. (2006)
Pismis 18	13:36:55	−62:05:36	6.85 ± 0.17	+12 ± 2	0.22 ± 0.04	1.20 ± 0.04	Piatti et al. (1998)
Trumpler 20	12:39:32	−60:37:36	6.86 ± 0.01	+134 ± 4	0.15 ± 0.07	1.50 ± 0.15	Donati et al. (2014)
Berkeley 44	19:17:12	+19:33:00	6.91 ± 0.12	+130 ± 20	0.27 ± 0.06	1.6 ± 0.3	Jacobson et al. (2016)
NGC 2420	07:38:23	+21:34:24	10.76		−0.13 ± 0.04	2.2 ± 0.3	Salaris et al. (2004), Sharma et al. (2006)
Berkeley 31	06:57:36	+08:16:00	15.16 ± 0.40	+340 ± 30	−0.27 ± 0.06	2.5 ± 0.3	Cignoni et al. (2011)
NGC 2243	06:29:34	−31:17:00	10.40 ± 0.20	+1200 ± 100	−0.38 ± 0.04	4.0 ± 1.2	Bragaglia & Tosi (2006)
M 67	08:51:18	+11:48:00	9.05 ± 0.20	+405 ± 40	−0.010 ± 0.04	4.3 ± 0.5	Salaris et al. (2004)
Berkeley 36	07:16:06	−13:06:00	11.30 ± 0.20	−40 ± 10	−0.16 ± 0.10	7.0 ± 0.5	Cignoni et al. (2011)

Notes. [a]Magrini et al. (2018).

5.2. Age re-determination with chemical clocks

To compare the two data sets, we compute the median abundance ratios of giant and subgiant star members in each cluster. In addition, since the abundances in GES are in the $12 + \log(X/H)$ form, we need to define our abundance reference to obtain abundances on the solar scale – in order to have the abundances in the [X/H] scale to compare with the solar-like stars. Table 8 shows three different sets of abundances: the solar abundances from iDR5 computed from archive solar spectra, the solar abundances by Grevesse et al. (2007), and the median abundances of giant stars in M 67. The cluster M 67 is known to have the same composition as the Sun (e.g. Randich et al. 2006; Pasquini et al. 2008; Önehag et al. 2014; Liu et al. 2016) and can there-

Table 8. Abundance references.

Element	Sun (iDR5)	Sun (Grevesse et al. 2007)	M 67 giants (iDR5)
MgI	7.51 ± 0.07	7.53 ± 0.09	7.51 ± 0.02(±0.05)
AlI	6.34 ± 0.04	6.37 ± 0.06	6.41 ± 0.01(±0.04)
SiI	7.48 ± 0.06	7.51 ± 0.04	7.55 ± 0.01(±0.06)
CaI	6.31 ± 0.12	6.31 ± 0.04	6.44 ± 0.01(±0.10)
TiI	4.90 ± 0.08	4.90 ± 0.06	4.90 ± 0.01(±0.09)
TiII	4.99 ± 0.07	–	5.01 ± 0.01(±0.10)
YII	2.19 ± 0.12	2.21 ± 0.02	2.15 ± 0.01(±0.09)

fore be used to confirm the abundance reference. The GES solar and M 67 abundances are in agreement with the reference

solar abundances from Grevesse et al. (2007). The average abundances for the three member giant stars in M 67 from the iDR5 recommended values are given together with their standard deviations and the typical errors on each measurement (in parenthesis; see third column of Table 8). In the following, we normalise our abundances to the M 67 abundances, as done in other GES consortium papers, such as Magrini et al. (2017, 2018) since most of the cluster member stars are giants. The median abundance ratios scaled to M 67 are shown in Table 9 where the uncertainties are the scatter errors on the median $(1.235 \cdot \sigma / \sqrt{N})$.

A large number of open clusters in our sample have ages younger than 1 Gyr, while our relations are derived from a sample of stars whose ages (from isochrone fitting) cannot be extended below 1 Gyr. We need to verify the possibility of extrapolating our relations towards the youngest regimes using solar-like stars with younger ages derived from independent methods. We adopt the literature ages for five solar-like stars analysed with our differential analysis. Their ages cannot be computed with our maximum-likelihood isochrone fitting since they are located close to the border of the YAPSI isochrone grid. Their ages are derived from the age of stellar associations to which they belong or they are calculated through gyrochronologic measurements: HD 1835 (600 Myr, in Hyades, Rosén et al. 2016), HIP 42333, HIP 22263 (0.3 ± 0.1 Gyr, 0.5 ± 0.1 Gyr, Aguilera-Gómez et al. 2018), HIP 19781 (in Hyades, Leão et al. 2019), HD 209779 (55 Myr, in IC 2391, Montes et al. 2001). In Fig. 6 we show the location of the five young solar-like stars with our sample of solar-like stars. These follow the same trend as the solar-like stars with ages >1 Gyr, demonstrating the continuity between the two samples and allowing us to extrapolate our relations up to 0.05 Gyr, the age of the youngest solar-like star in the sample.

In Fig. 7, we show the abundance ratios of the solar-like stars versus age, together with those of OCs in the metallicity bin of −0.4 < [Fe/H] < +0.3 (range of cluster metallicity). The two populations follow similar trends. However, some of the youngest open clusters are located outside the distribution of the solar-like stars. In particular, this different behaviour is highlighted in Fig. 8, where we compare their literature ages with the age obtained from our relations in Table 6. We use the general formula Age = $c' + x'_1 \cdot$ [Fe/H] + $x'_2 \cdot$ [A/B], where [Fe/H] and [A/B] of OCs are known. There is a group of clusters for which the agreement with most of the chemical clocks is good. Most of these clusters are located at $R_{GC} > 7$ kpc, except for the outermost cluster, Berkeley 31. The cluster lies at $R_{GC} \sim 15$ kpc and its age derived with the stellar dating relations is slightly higher than the literature values (except for [Y/Ca]). On the other hand, the ages derived for the innermost OCs at $R_{GC} < 7$ kpc are higher than their literature age values or are negative in a few cases (not reliable ages). We recall that our stellar dating relations already take into account the dependence on [Fe/H].

To understand our failure to reproduce the ages of clusters located far from the solar neighbourhood, we vary the form of the multivariate linear regressions shown in the Sect. 4.2, adding a term containing $x_3 \cdot$ [Fe/H] · Age. This term takes into account the dependence of age on the metallicity. The addition of this term is not sufficient to reconcile the ages derived from the chemical clocks with the literature ages for the inner disc open clusters.

Indeed, in Fig. 9 we present the residuals of the regression for [Y/Mg] as a function of [Fe/H]. There is a similar scatter on the residuals both for solar-like stars (the density contour) and open clusters (marked with the star symbol), colour-coded by their

Galactocentric distance. However, OCs with $R_{GC} < 7$ kpc have larger age residuals than the other clusters or solar-like stars, as mentioned above.

Moreover, we calculate the Y abundances using the photometric log g computed in Sect. 2.4 in order to verify its effect on our results since the yttrium abundances derived from YII lines are sensitive to gravity. The median difference between spectroscopic gravities and the photometric ones is +0.02 dex in the solar metallicity regime (−0.1 < [Fe/H] < 0.1) and −0.015 dex in the super-solar regime ([Fe/H] > 0.1). These differences produce a median difference in [Y/H] of +0.01 dex and −0.01 dex in the two respective regimes, a negligible effect for our purpose. We calculate the chemical ages applying the multivariate linear regression as explained in Sect. 4.2 with the Y abundances deduced by photometric log g, finding no significant variation with respect to the chemical ages obtained using the spectroscopic log g. In the following section, we discuss some hypotheses capable of explaining this discrepancy.

6. The non-universality of the relations between ages and abundance ratios involving *s*-process elements

The aim of the present study, together with other previous works (e.g. Feltzing et al. 2017; Spina et al. 2018; Delgado Mena et al. 2019, among many others), is to find stellar dating relations between ages and some abundance ratios that are applicable to the whole Galaxy, or at least to vast portions of it. The opening questions in Feltzing et al. (2017) focus on the possible universality of the correlation between for example [Y/Mg] and age found in a sample of the solar-like stars, and, if it holds, also for larger ranges of [Fe/H], or for stars much further than the solar neighbourhood or in different Galactic populations, such as those in the thick disc.

As we mention in Sect. 3, *s*-processes occur in low- and intermediate-mass AGB stars (see, e.g. Busso et al. 2001; Karakas & Lugaro 2016), with timescales ranging from less than a gigayear to several gigayears for the higher and lower mass AGB stars, respectively. On the other hand, α elements (in different percentages) are produced by core-collapse supernovae during the final stages of the evolution of massive stars on shorter timescales. Combining the enrichment timescales of the *s*-process and α-elements, younger stars are indeed expected to have higher [s/α] ratios than older stars. However, the level of [s/α] reached in different parts of the Galaxy at the same epoch is not expected to be the same. Enlarging the sample of stars or star clusters outside the solar neighbourhood means that we have to deal with the complexity of the Galactic chemical evolution. This includes radial variation of the star formation history (SFH) in the disc driven by an exponentially declining infall rate and a decreasing star formation efficiency towards the outer regions (see, e.g. Magrini et al. 2009, and in general, multi-zone chemical evolution models). Consequently, different radial regions of the disc experience different SFHs, which produce different distributions in age and metallicity of the stellar populations. At each Galactocentric distance, the abundance of unevolved stars, which inherited heavy nuclei from the contributions of previous generations of stars, is thus affected by the past SFH. Last but not least, there is a strong metallicity dependence of the stellar yields. The metallicity dependence of the stellar yield is particularly important for neutron-capture elements produced through the *s*-process. Indeed, being secondary elements, the production of the *s*-process elements strongly depends on the quantity of

Table 9. Abundance ratios of open clusters in the GES sample.

Cluster	# stars	[Y/Mg] (dex)	[Y/Al] (dex)	[Y/TiI] (dex)	[Y/TiII] (dex)	[Y/Ca] (dex)	[Y/Si] (dex)
Berkeley 31	5 (G)	−0.01 ± 0.03	0.02 ± 0.03	0.01 ± 0.04	−0.07 ± 0.04	0.06 ± 0.04	0.03 ± 0.04
Berkeley 36	5 (G)	−0.05 ± 0.06	−0.07 ± 0.06	0.00 ± 0.07	−0.04 ± 0.07	0.13 ± 0.06	−0.02 ± 0.06
Berkeley 44	7 (G)	0.14 ± 0.07	0.19 ± 0.07	0.13 ± 0.08	−0.04 ± 0.14	0.26 ± 0.07	0.18 ± 0.07
Berkeley 81	13 (G)	0.09 ± 0.03	0.07 ± 0.03	0.13 ± 0.05	0.17 ± 0.05	0.19 ± 0.04	0.08 ± 0.04
M 67	3 (G)	0.00 ± 0.01	0.00 ± 0.01	0.00 ± 0.01	0.00 ± 0.01	0.00 ± 0.01	0.00 ± 0.01
Melotte 71	4 (G)	0.07 ± 0.01	0.15 ± 0.01	0.13 ± 0.02	0.09 ± 0.01	0.03 ± 0.01	0.09 ± 0.03
NGC 2243	17 (16 G, 1 SG)	−0.04 ± 0.03	0.00 ± 0.03	0.00 ± 0.05	−0.04 ± 0.04	−0.02 ± 0.09	−0.01 ± 0.03
NGC 2420	28 (24 G, 4 SG)	0.07 ± 0.03	0.13 ± 0.03	0.08 ± 0.03	0.04 ± 0.03	0.07 ± 0.03	0.08 ± 0.03
NGC 4815	6 (G)	0.11 ± 0.09	0.16 ± 0.08	0.19 ± 0.10	0.10 ± 0.08	0.12 ± 0.09	0.08 ± 0.07
NGC 6005	9 (G)	−0.01 ± 0.02	0.02 ± 0.02	0.03 ± 0.03	0.02 ± 0.02	0.05 ± 0.02	−0.05 ± 0.02
NGC 6067	12 (G)	0.08 ± 0.04	0.03 ± 0.05	0.06 ± 0.05	0.13 ± 0.04	0.05 ± 0.07	0.02 ± 0.04
NGC 6259	12 (G)	−0.05 ± 0.02	−0.05 ± 0.02	0.00 ± 0.04	0.07 ± 0.03	0.04 ± 0.02	−0.08 ± 0.02
NGC 6633	3 (G)	0.08 ± 0.02	0.18 ± 0.02	0.19 ± 0.02	0.11 ± 0.01	0.09 ± 0.01	0.07 ± 0.01
NGC 6705	28 (G)	−0.03 ± 0.03	−0.10 ± 0.03	0.05 ± 0.04	0.08 ± 0.04	0.02 ± 0.04	−0.09 ± 0.03
NGC 6802	10 (G)	0.17 ± 0.02	0.14 ± 0.02	0.23 ± 0.03	0.10 ± 0.02	0.24 ± 0.02	0.13 ± 0.02
Rup 134	16 (G)	−0.08 ± 0.02	−0.08 ± 0.02	−0.03 ± 0.02	−0.04 ± 0.02	0.04 ± 0.02	−0.14 ± 0.02
Pismis 18	6 (G)	0.05 ± 0.04	0.10 ± 0.04	0.13 ± 0.04	0.06 ± 0.04	0.12 ± 0.04	0.00 ± 0.04
Trumpler 20	34 (G)	0.12 ± 0.02	0.16 ± 0.02	0.17 ± 0.02	0.08 ± 0.02	0.15 ± 0.02	0.04 ± 0.02
Trumpler 23	10 (G)	−0.05 ± 0.04	−0.02 ± 0.04	0.05 ± 0.06	0.01 ± 0.04	0.11 ± 0.05	−0.10 ± 0.04

Notes. G: giants, SG: sub-giants.
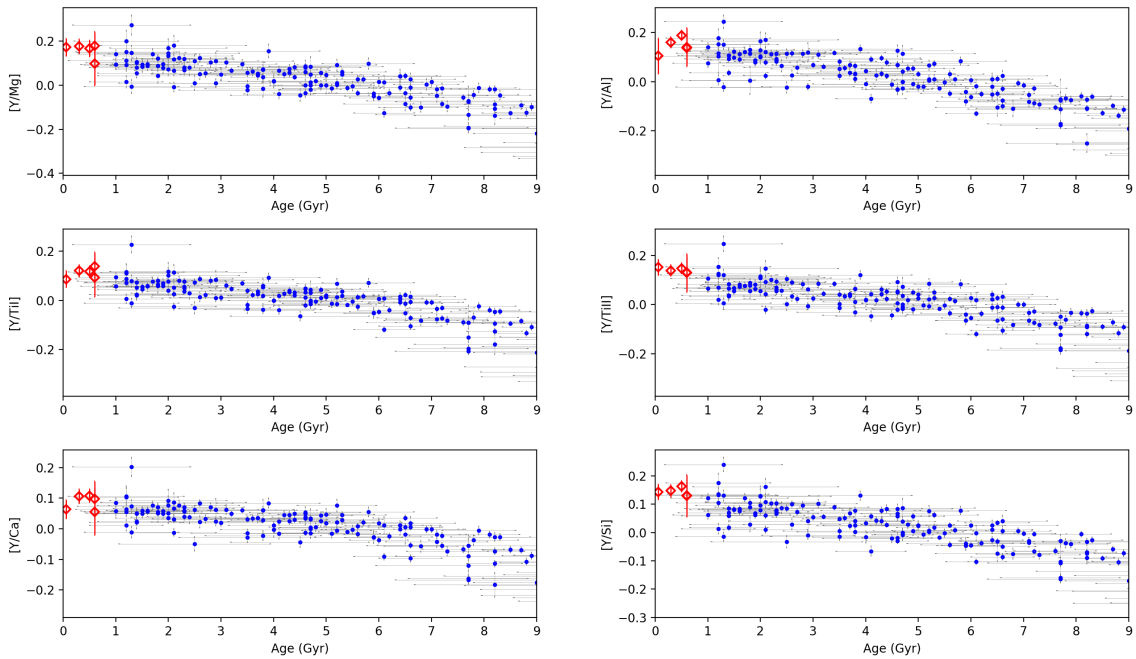
Fig. 6. Abundance ratio vs. stellar age. The blue dots are our sample of solar-like stars and the red diamonds represent the five solar-like stars with ages from the literature and abundances from our analysis.

seeds (iron) present in the star. However, at high metallicity the number of iron seeds is much larger than the number of neutrons. Consequently, in the super-solar metallicity regime, a less effective production of neutron-capture elements with respect to iron is predicted (Busso et al. 2001; Karakas & Lugaro 2016). In addition, at high metallicity there might be a lower number of thermal pulses during the AGB phase, with a consequent lower final yield of s-process elements (see, e.g. Goriely & Siess 2018). Moreover, the production of Mg also depends on metallicity, in particular at high [Fe/H] where stellar rotation during the latest phases of the evolution of massive stars increases the yield of Mg (Romano

et al. 2010; Magrini et al. 2017). The interplay between the stellar yield and the metallicity of progenitors produces a different evolution at different Galactocentric distances.

The combination of these dependencies points toward a relation between [Y/Mg], or in general [s/α], and age that changes with Galactocentric distance. Following the suggestions of Feltzing et al. (2017), we first study the stellar dating relations from chemical clocks for a sample of the solar-like stars in the solar neighbourhood, considering a large metallicity range to investigate their metallicity dependence. This was discussed in Sect. 4.
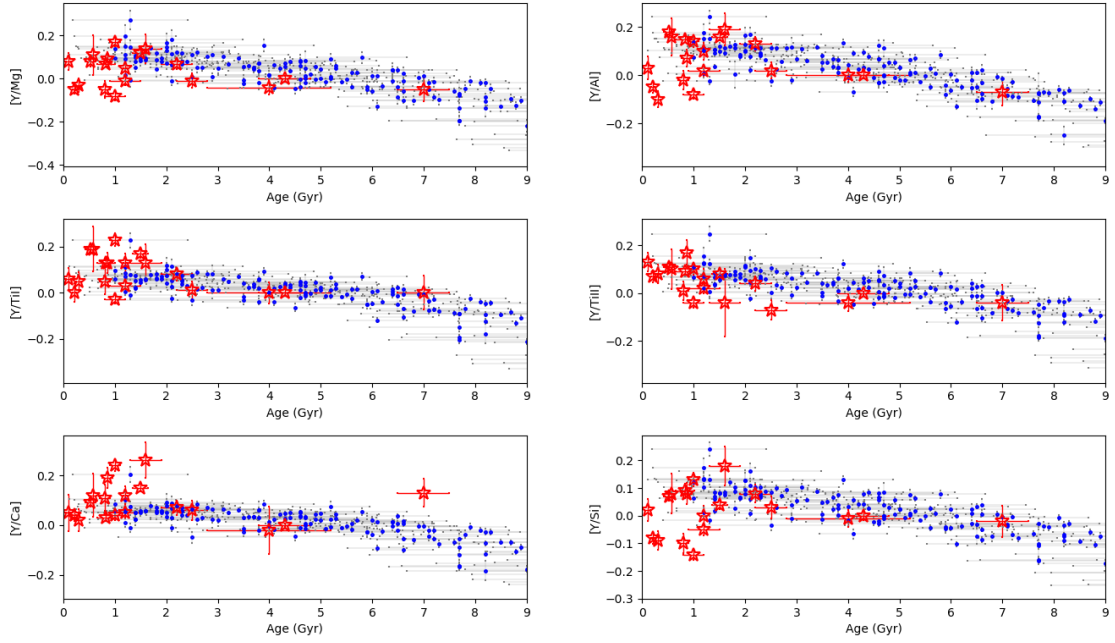
Fig. 7. Abundance ratio vs. stellar age. The blue dots show the values of our solar-like stars and the red stars represent the mean values for the open clusters in the GES sample.
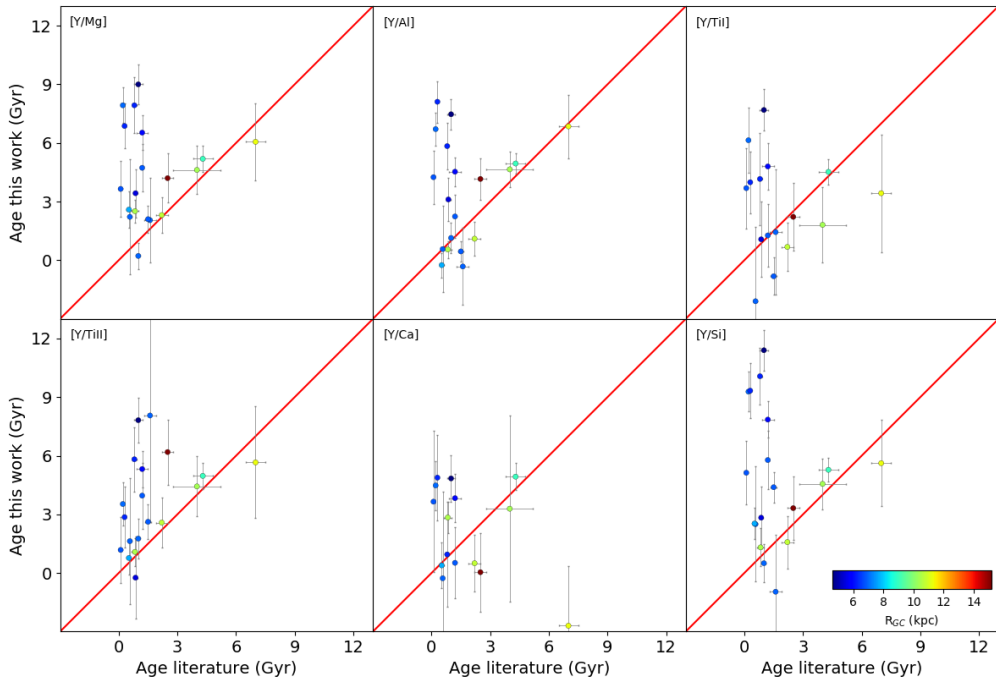

Fig. 8. Comparison between the ages from the literature and the ages inferred in the present work for the open clusters. The symbols are colour-coded by their Galactocentric distances. We note that we only show positive upper limit ages in this plot.

Here, we present the analysis of stars located far away from the solar neighbourhood using a sample of open clusters observed by the *Gaia*-ESO with a precise determination of age and distance. The sample gives us important indications on the variation of the $[s/\alpha]$ in different parts of the Galaxy. In Fig. 10, we present different abundance ratios in OCs, including yttrium, as a function of Galactocentric distance R_{GC}. The ratio $[s/\alpha]$ decreases with decreasing Galactocentric radii for $R_{GC} < 6$ kpc, exhibits a maximum around the solar radius (except for [Y/Ca]) and then shows a slight decrease with increasing distance for $R_{GC} > 9$ kpc. Moreover, along the OC

data, we also plot the *Gaia*-ESO samples of inner disc stars (labeled with GE_MW_BL in the GES survey) and those from the solar neighbourhood (GE_MW). We calculate their Galactocentric distances from coordinates RA, Dec, and parallaxes of *Gaia* DR2 as explained in Sect. 2.5. Field stars show a behaviour that is similar to that of the OCs, with a lower [Y/Mg] for the inner Milky Way populations (i.e. for $R_{GC} < 8$ kpc). It is interesting to notice that in the inner disc, the bulk of field stars, usually older than stars in clusters, show an even lower $[s/\alpha]$ than the open cluster stars.
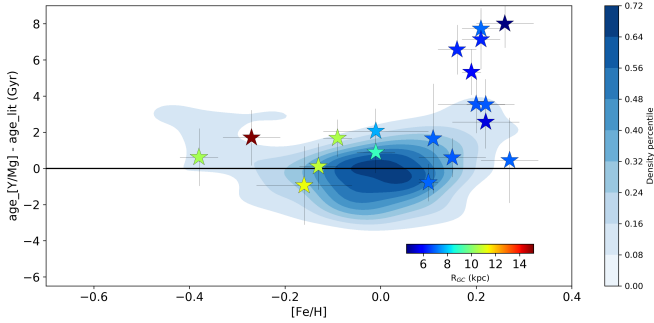
Fig. 9. Residuals between the chemical-clock ages from [Y/Mg] and the literature ages as a function of [Fe/H]. The contours represent the density of the sample of solar-like stars, while the stars represent the open clusters, colour-coded by R_{GC}.

6.1. The overproduction of s-process elements at high [Fe/H]

As shown in the previous sections, stars with the same age but located in different regions of the Galaxy have different composition. Thus, the stellar dating relations between abundance ratios and stellar ages based on a sample of stars located in limited volumes of the Galaxy cannot be easily translated into general stellar dating relations valid for the whole disc.

The driving reason for this is that the SFH strongly effects the abundances of the s-process elements and the yields of low- and intermediate-mass stars depend non-monotonically on the metallicity (Feltzing et al. 2017). This effect was already noticed by Magrini et al. (2018, see their Fig 11), where [Y/Ba] versus age was plotted in different bins of metallicity and Galactocentric distance. The innermost bin, dominated by metal rich stars, shows a different behaviour with respect to the bins located around the solar location.

We include the literature s-process yields (see, e.g. Busso et al. 2001; Maiorca et al. 2012; Cristallo et al. 2011; Karakas & Lugaro 2016) in our Galactic Chemical Evolution (GCE) model (Magrini et al. 2009). In Fig. 11, we show, as an example, the results of the chemical evolution of Magrini et al. (2009) in which we have adopted the yields of Maiorca et al. (2012). The three curves give the relations between stellar age and [Y/Mg] at three different Galactocentric distances (inner disc, solar neighbourhood, and outer disc). The GCE models at R_{GC} of 9 kpc and 16 kpc show a similar trend and reproduce the pattern of OCs and solar-like stars very well. The agreement is completely lost at R_{GC} = 6 kpc, where the faster enrichment of the inner disc for GCE produces a higher [Y/Mg], which is not observed in the open clusters. Similar results are obtained adopting the yields from the FRUITY database (Domínguez et al. 2011; Cristallo et al. 2011), and from the Monash group (Lugaro et al. 2012; Fishlock et al. 2014; Karakas et al. 2014, 2018; Shingles et al. 2015; Karakas & Lugaro 2016) in the GCE. As shown in Fig. 12, in which the yields of yttrium Y are shown in different bins of metallicity Z for different stellar masses (1.3, 1.5, 2, 2.5, 3, 4, 5 $M_\odot$), we can see that in the first two sets of yields the production of s-process elements increases at high metallicity. This produces an increasing abundance of s-process elements in the inner disc, which is not observed in the abundances of the open cluster sample. The yields by Maiorca et al. (2012) have a flatter trend with the metallicity, which is not able to reproduce the behavior of open clusters with R_{GC} < 7 kpc. A similar result is shown in Griffith et al. (2019), where the median trends of Y, Ba, and La exhibit peaks near solar [Mg/H] and plateaus at low metallicity, and a decreasing trend at high [Mg/H]. These latter authors explain their finding as the result of a metallicity dependence on AGB yields, but they do not consider the different SFH of each radial region of the Galaxy.

6.2. A suggestion for the need for new s-process yields at high metallicity

We investigate which set of *empirical* yields is necessary to reproduce the observed lower trends, i.e. [Y/Mg] or [Y/Al] versus age, in the inner disc than in the solar neighbourhood. The s-process element yields depend on the metallicity in two different ways; that is, they depend (i) on the number of iron nuclei as seeds for the neutron captures, and (ii) on the flux of neutrons. The former decreases with decreasing metallicity, while the latter increases because the main neutron source – ^{13}C – is a primary process. ^{13}C is produced by mixing protons into the He-shell present in low-mass AGB stars, where they are captured by the abundant ^{12}C, which itself is produced during the 3α process (also a primary process). This means that the amount of ^{13}C does not depend on the metallicity. The neutron flux depends (approximately) on $^{13}C/^{56}Fe$, which increases with decreasing metallicity. This means there are more neutrons per seed in low-metallicity AGB stars and less in high-metallicity AGB stars (see Busso et al. 2001; Karakas & Lugaro 2016). Consequently, we should expect less s-process elements to be produced at high metallicity.

We tested a set of yields to investigate their behaviour at high metallicity. Yields for subsolar metallicities were left unchanged from their Maiorca et al. (2012) values, while we depressed the yields at super-solar metallicity by a factor of ten. In Fig. 13, we show the time evolution of [Y/Mg] in three radial regions of our Galaxy adopting our *empirical* yields for Y. The curves at 9 and 16 kpc are the same as those shown in Fig. 11 computed with the original yields of Maiorca et al. (2012), while the curve at R_{GC} = 6 kpc is affected by the depressed yields at high metallicity. If the Y production in those regions was indeed less efficient with respect to the production of Mg, we would therefore have a lower [Y/Mg]. Clearly, this is simply an empirical suggestion that needs a full new computation of stellar yields for low- and intermediate-mass AGB stars. However, there are also other possibilities, such as for instance the adoption of yields for Mg and Y that take into account the stellar rotation in massive stars; these yields are higher at high metallicity because of a more efficient rotation. The rotating massive stars produce the s-process elements preferentially at the first peak (Sr, Y and Zr) during the hydrostatic phase, and then expel the elements at collapse, suggesting that the production of Y and Mg might be coupled. The combined production of Y and Mg might produce a global flattening in the trend of [Y/Mg] versus age at high-metallicity. An exhaustive discussion of the origin of the change of slope of the relation between [Y/Mg] and age is outside the scope of the present paper. However, it is clear that a revision of the s-process yields at high metallicity is necessary to explain the current data.

7. Application to field stars

We conclude that the stellar dating relations from chemical clocks derived through a multivariate linear regression in Sect. 4.2 are not valid throughout the whole Galaxy, but can only be applied in the solar neighbourhood. A natural application of our stellar dating relations is to the high-resolution sample of solar neighbourhood stars observed with UVES by the *Gaia*-ESO (see Stonkute et al. 2016, for the definition of the target selection). The selection of stars in a limited volume close to the
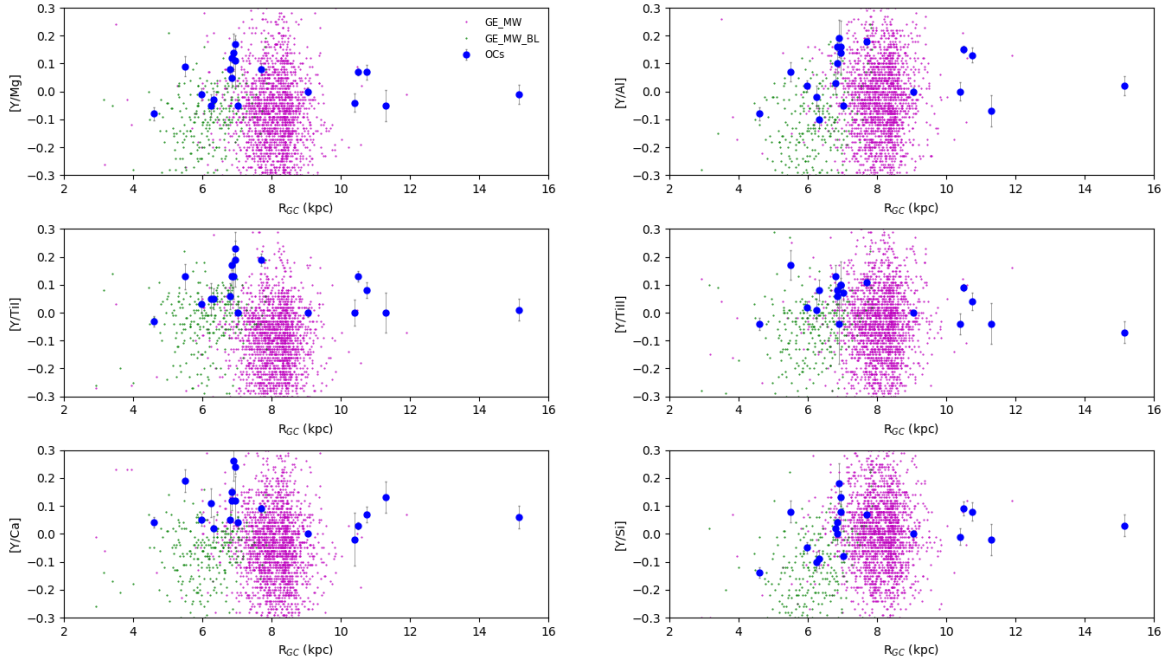
Fig. 10. Chemical clocks, including yttrium, as a function of Galactocentric distance. The filled circles represent the open clusters, while the small dots represent field stars in the solar neighbourhood (magenta) and in the inner regions of the disc (green).
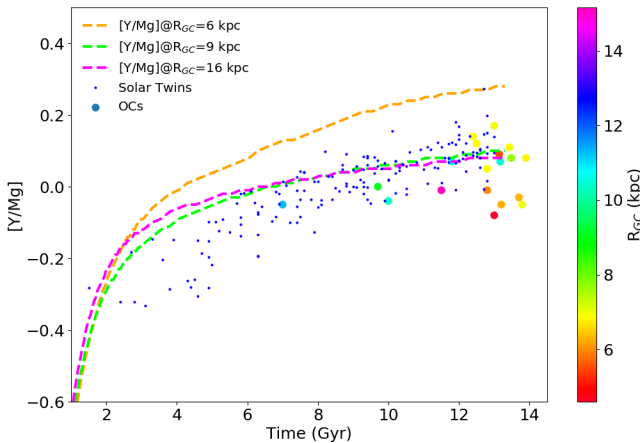
Fig. 11. [Y/Mg] vs. time of Galactic evolution. The lines represent the chemical evolution models computed to different Galactocentric distances. The small blue dots are the solar-like stars, while the filled circles, colour-coded by R_{GC}, are the open clusters.

Sun allows us to use the relations built from our solar-like stars located in a similar region.

We select stars present in the *Gaia*-ESO survey with the GES_TYPE "GE_MW", that is stars belonging to the solar neighbourhood. This sample is mainly composed of stars in the evolutionary phases around the turn-off. For each of them, we derived their age using the stellar dating relation Age = 5.245 + 5.057 · [Fe/H] − 32.546 · [Y/Mg], where [Fe/H] and [Y/Mg] are known from the GES survey. Figure 14 shows [Mg/Fe] versus [Fe/H] for this sample in the range of metallicity of our solar-like stars, −0.7 ≤ [Fe/H] ≤ 0.4, where each field star is colour-coded by its age. There is a clear dichotomy between thin- and thick-disc stars and an evident gradient in age along the thin disc, as already shown by Titarenko et al. (2019), who traced the differences between the two discs with [Y/Mg]. The oldest stars are present in high-α thick disc, while the youngest

stars are located in the thin disc. The average age of thin-disc stars increases with decreasing [Fe/H] and increasing [Mg/Fe]. We obtained a similar result in Casali et al. (2019), where we calculated the age of giant field stars present in APOGEE DR14 and GES using the stellar dating relation age–[C/N] (see our Fig. 13, where we plot [α/Fe] vs. [Fe/H] colour-coded by age). We recall indeed that in Casali et al. (2019), the stars colour-coded by age deduced from the [C/N] ratio for each of them are well-separated in age between thin and thick disc, confirming different timescales and SFHs for the two discs.

This dichotomy is also clear if we plot [Mg/Fe] as a function of the age inferred in this work using the dating relation [Y/Mg]–[Fe/H]–age. In Fig. 15, we can see how stars up to 8 Gyr show a similar content of [Mg/Fe] around the solar value, while beyond 8 Gyr their [Mg/Fe] ratios begin to increase with increasing age (Bensby et al. 2014). This difference in [Mg/Fe] clearly represents the dichotomy between thin and thick disc, where stars with an approximately solar [Mg/Fe] value belonging to the thin disc are younger than [Mg/Fe]-rich stars lying in the thick disc. In particular, the slope changes about 8 Gyr ago, during the epoch where the thin disc started to form (Bensby et al. 2014; Helmi et al. 2018).

8. Summary and conclusions

In this work, we present the differential line-by-line analysis of high-quality HARPS spectra of a sample of solar-like stars (with parameters close to the solar ones for T_{eff} and log g), with metallicity [Fe/H] spanning from −0.7 to +0.4 dex. We obtain precise estimates of their atmospheric parameters (T_{eff}, log g, [Fe/H] and ξ) and abundances of 25 elements and/or ions (24 abundance ratios over iron). We derive their ages through isochrone fitting.
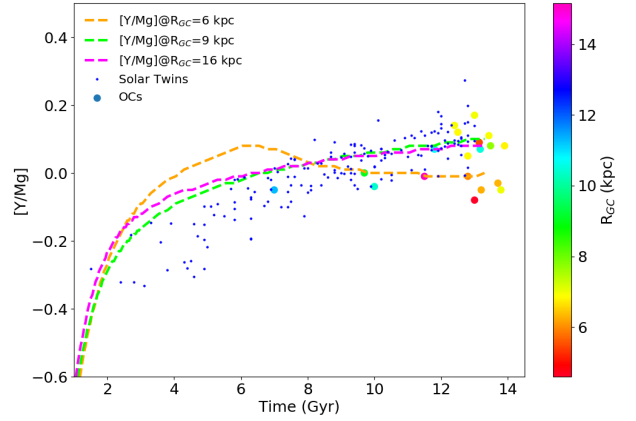
We investigate the relations between [X/Fe] and stellar age, confirming strong correlations between [X/Fe] and stellar age for the s-process (negative slope) and α-elements (positive slope), while for the iron-peak elements the relations are nearly flat.
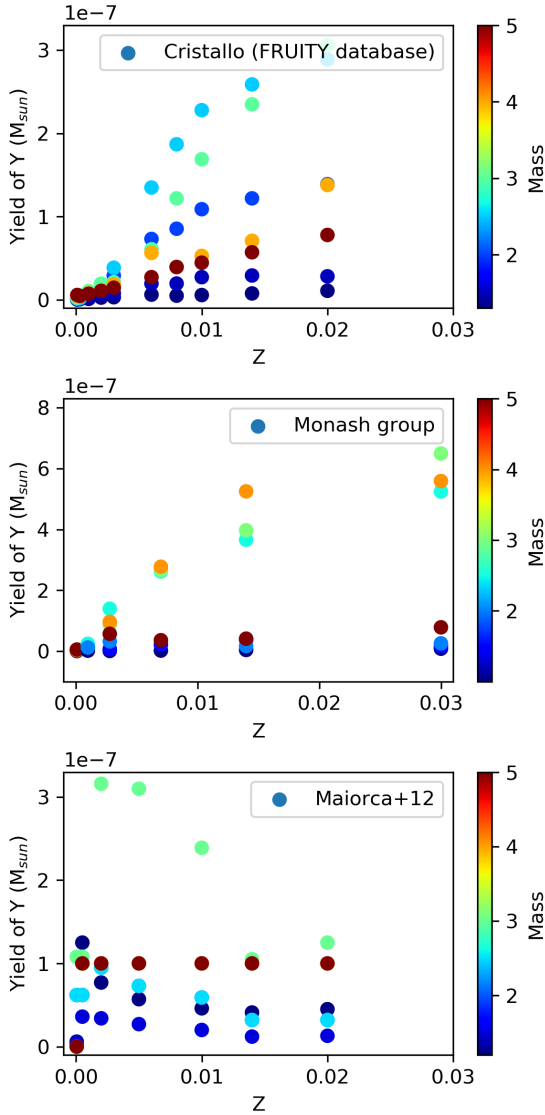
Fig. 12. Comparison of yields of Y from the FRUITY database, the Monash group, and Maiorca et al. (2012) as a function of metallicity Z. The circles are colour-coded by stellar mass.


Fig. 13. [Y/Mg] vs. time of Galactic evolution. The lines represent the chemical evolution models computed to different Galactocentric distances where the stellar yields are suppressed. Symbols as in Fig. 11.

We select the best abundance ratios (higher correlation coefficients), which are usually the ratios involving an *s*-element and an *α*-element. We perform a multivariate linear regression for 17 different ratios taking into account the metallicity dependence. We compare our results with the literature, finding good agreement.

To check the validity of our relations outside the solar neighbourhood, we apply them to the sample of open clusters in the *Gaia*-ESO survey located at a wide range of Galactocentric distances $4\,\mathrm{kpc} < R_{GC} < 16\,\mathrm{kpc}$. The literature ages obtained from isochrone fitting of the full cluster sequence of clusters located at $R_{GC} > 7\,\mathrm{kpc}$ are in good agreement, on average, with the ages derived from our stellar dating relations. On the other hand, the ages derived for the innermost OCs at $R_{GC} < 7\,\mathrm{kpc}$ are much older than the literature ones. This different behaviour points towards different [s/α]–[Fe/H]–age relations depending on the location in the disc. In principle, we might expect that, combining the enrichment timescales of the *s*-process and *α*-elements, younger stars should have higher [s/α] ratios than older ones. However, this does not happen everywhere in the disc in the same way: [s/α] for the youngest and most metal-rich stars in

the inner regions is lower than that of stars in the solar neighbourhood with similar ages. This discrepancy might be related to two different aspects: (i) the different SFHs, with a consequently different distribution in age and metallicity of the stellar populations in each region, and (ii) the strong and non-monotonic metallicity dependence of the *s*-process stellar yields. The latter is related to the secondary nature of the *s*-process elements, whose yields depend on the number of iron seeds and on the flux of neutrons.

The *s*-process yields present in the literature (Maiorca et al. 2012; Karakas & Lugaro 2016; Cristallo et al. 2011) are not able to reproduce the Y abundances of stars and star clusters in the inner disc. We investigate the use of a set of empirical yields introduced in our GCE model for the Milky Way (Magrini et al. 2009) to reproduce the observed trends, namely a lower [s/α] in the inner disc than in the solar neighbourhood. To reproduce the inner disc clusters, a reduced production of yttrium by a factor of ten at high metallicity is required. Another possibility could be to include stellar rotations in massive stars, which might affect both *s*-process and Mg abundances at high metallicity.

Finally, we apply our [Y/Mg]–[Fe/H]–age relation to the field stars observed with UVES in the *Gaia*-ESO survey, specifically those located in the solar neighbourhood, in order to derive their ages. The ages derived with our relation confirm the dichotomy in age between the thin and thick disc, as shown in the [Mg/Fe] versus [Fe/H] plane, similar to what was found in Casali et al. (2019). This immediate application confirms the potential power of chemical clocks to improve our knowledge of stellar ages.

With the present work, we confirm the existence of several relations between abundance ratios and stellar ages. These relations have a secondary dependence on metallicity, which can be taken into account. These relations, built from a sample of stars located in the solar neighbourhood, cannot be applied to star clusters located in regions of the Galaxy with different SFH, in particular in the inner disc. The [Y/Mg]–[Fe/H]-age relation, and similar relations involving *s*-process elements and *α*-elements, are not universal. Their form depends on the location in the Galaxy. The reasons for this may be found in the differences in the SFHs (peaks of the age and metallicity distribution function) and in the non-monotonic dependence of the *s*-process yields on metallicity. A better understanding of the *s*-process in the supersolar-metallicity regime in low- and intermediate-mass AGB stars is indeed also necessary to clarify the use
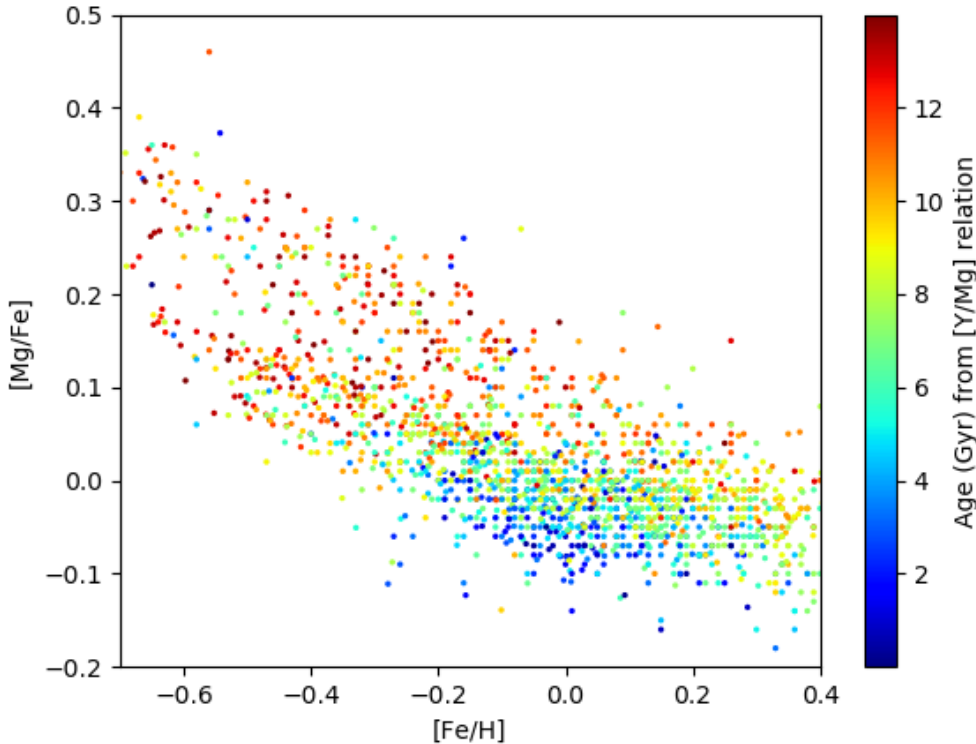
Fig. 14. [Mg/Fe] vs. [Fe/H] of solar neighbourhood stars present in the *Gaia*-ESO. The stars are colour-coded according to their age computed with the stellar dating relation [Y/Mg]–[Fe/H]–age.
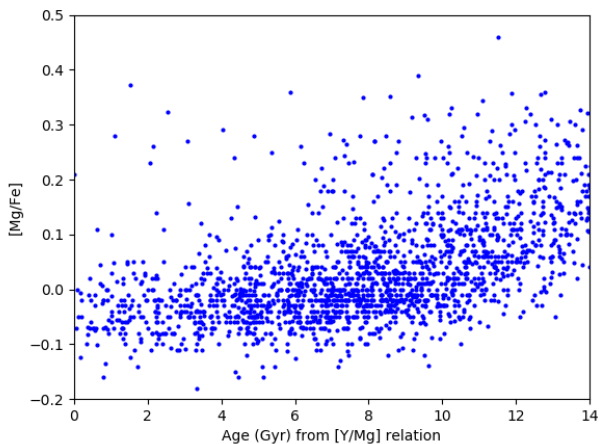
Fig. 15. [Mg/Fe] vs. age of solar neighbourhood stars present in the *Gaia*-ESO deduced from the stellar dating relation [Y/Mg]–[Fe/H]–age.

of abundance ratios as chemical clocks. This failure of the employment of the chemical clocks to determine the stellar ages does not concern another important age indicator, the [C/N] ratio (Casali et al. 2019). The latter is related to stellar evolution, and only to a minor extent to global Galactic evolution.

References

Aguilera-Gómez, C., Ramírez, I., & Chanamé, J. 2018, A&A, 614, A55
Alonso-Santiago, J., Negueruela, I., Marco, A., et al. 2017, MNRAS, 469, 1330
Asplund, M. 2005, ARA&A, 43, 481
Ayres, T. R., Plymate, C., & Keller, C. U. 2006, ApJS, 165, 618
Bailer-Jones, C. A. L., Rybizki, J., Fouesneau, M., Mantelet, G., & Andrae, R. 2018, AJ, 156, 58
Bedell, M., Meléndez, J., Bean, J. L., et al. 2014, ApJ, 795, 23
Bedell, M., Bean, J. L., Meléndez, J., et al. 2018, ApJ, 865, 68
Bensby, T., Feltzing, S., Lundström, I., & Ilyin, I. 2005, A&A, 433, 185
Bensby, T., Feltzing, S., & Oey, M. S. 2014, A&A, 562, A71
Bland-Hawthorn, J., Sharma, S., Tepper-Garcia, T., et al. 2019, MNRAS, 486, 1167
Bovy, J. 2015, ApJS, 216, 29
Bragaglia, A., & Tosi, M. 2006, AJ, 131, 1544
Busso, M., Gallino, R., Lambert, D. L., Travaglio, C., & Smith, V. V. 2001, ApJ, 557, 802
Cantat-Gaudin, T., Vallenari, A., Zaggia, S., et al. 2014, A&A, 569, A17
Carraro, G., Janes, K. A., Costa, E., & Méndez, R. A. 2006, MNRAS, 368, 1078
Castelli, F., & Kurucz, R. L. 2004, A&A, 419, 725
Casali, G., Magrini, L., Tognelli, E., et al. 2019, A&A, 629, A62
Cignoni, M., Beccari, G., Bragaglia, A., & Tosi, M. 2011, MNRAS, 416, 1077

Cristallo, S., Piersanti, L., Straniero, O., et al. 2011, ApJS, 197, 17
Cui, X.-Q., Zhao, Y.-H., Chu, Y.-Q., et al. 2012, Res. Astron. Astrophys., 12, 1197
da Silva, R., de Porto Mello, G.F., & Milone, A.C. 2012, A&A, 542, A84
De Silva, G. M., Freeman, K. C., Bland-Hawthorn, J., et al. 2015, MNRAS, 449, 2604
Delgado Mena, E., Moya, A., Adibekyan, V., et al. 2019, A&A, 624, A78
Deng, L.-C., Newberg, H. J., Liu, C., et al. 2012, Res. Astron. Astrophys., 12, 735
Domínguez, I., Cristallo, S., Straniero, O., et al. 2011, in The Fruity Database: Chemical Features of Low-Mass AGB Stars, ed. F. Kerschbaum, T. Lebzelter, & R. F. Wing, 57
Donati, P., Cantat Gaudin, T., Bragaglia, A., et al. 2014, A&A, 561, A94
Epstein, C. R., Johnson, J. A., Dong, S., et al. 2010, ApJ, 709, 447
Feltzing, S., Fohlman, M., & Bensby, T. 2007, A&A, 467, 665
Feltzing, S., Howes, L. M., McMillan, P. J., & Stonkute, E. 2017, MNRAS, 465, L109
Fishlock, C. K., Karakas, A. I., Lugaro, M., & Yong, D. 2014, ApJ, 797, 44
Friel, E. D., Donati, P., Bragaglia, A., et al. 2014, A&A, 563, A117
Gaia Collaboration (Brown, A. G. A., et al.) 2018, A&A, 616, A1
Gilmore, G., Randich, S., Asplund, M., et al. 2012, The Messenger, 147, 25
Goriely, & Siess, L. 2018, A&A, 609, A29
Grevesse, N., Asplund, M., & Sauval, A. J. 2007, Space Sci. Rev., 130, 105
Griffith, E., Johnson, J. A., & Weinberg, D. H. 2019, ApJ, 886, 84
Hatzidimitriou, D., Held, E. V., Tognelli, E., et al. 2019, A&A, 626, A90
Haywood, M., Di Matteo, P., Lehnert, M. D., Katz, D., & Gómez, A. 2013, A&A, 560, A109
Helmi, A., Babusiaux, C., Koppelman, H. H., et al. 2018, Nature, 563, 85
Jacobson, H. R., Friel, E. D., Jílková, L., et al. 2016, A&A, 591, A37
Jofré, P., Jackson, H., & Tucci Maia, M. 2020, A&A, 633, L9
Jurić, M., Ivezić, Ž., Brooks, A., et al. 2008, ApJ, 673, 864
Karakas, A. I., & Lugaro, M. 2016, ApJ, 825, 26
Karakas, A. I., Marino, A. F., & Nataf, D. M. 2014, ApJ, 784, 32
Karakas, A. I., Lugaro, M., Carlos, M., et al. 2018, MNRAS, 477, 421
Leão, I. C., Pasquini, L., Ludwig, H. G., & de Medeiros, J. R. 2019, MNRAS, 483, 5026
Lindegren, L., Hernández, J., Bombrun, A., et al. 2018, A&A, 616, A2
Liu, F., Asplund, M., Yong, D., et al. 2016, MNRAS, 463, 696
Lugaro, M., Karakas, A. I., Stancliffe, R. J., & Rijs, C. 2012, ApJ, 747, 2
Magrini, L., Sestito, P., Randich, S., & Galli, D. 2009, A&A, 494, 95
Magrini, L., Randich, S., Donati, P., et al. 2015, A&A, 580, A85
Magrini, L., Randich, S., Kordopatis, G., et al. 2017, A&A, 603, A2
Magrini, L., Spina, L., Randich, S., et al. 2018, A&A, 617, A106
Maiorca, E., Magrini, L., Busso, M., et al. 2012, ApJ, 747, 53
Majewski, S. R., Schiavon, R. P., Frinchaboy, P. M., et al. 2017, AJ, 154, 94
Masseron, T., & Gilmore, G. 2015, MNRAS, 453, 1855
Matteucci, F. 2014, The Origin of the Galaxy and Local Group, Saas-Fee Advanced Course (Berlin Heidelberg: Springer-Verlag), 37, 145
Mayor, M., Pepe, F., Queloz, D., et al. 2003, The Messenger, 114, 20
Meléndez, J., & Ramírez, I. 2007, ApJ, 669, L89
Meléndez, J., Dodds-Eden, K., & Robles, J. A. 2006, ApJ, 641, L133
Meléndez, J., Asplund, M., Gustafsson, B., & Yong, D. 2009, ApJ, 704, L66
Meléndez, J., Ramírez, I., Karakas, A. I., et al. 2014, ApJ, 791, 14
Mermilliod, J.-C., Clariá, J. J., Andersen, J., Piatti, A. E., & Mayor, M. 2001, A&A, 375, 30
Montes, D., López-Santiago, J., Gálvez, M. C., et al. 2001, MNRAS, 328, 45
Nagar, T., Spina, L., & Karakas, A. I. 2020, ApJ, 888, L9
Nissen, P. E. 2015, A&A, 579, A52
Nissen, P. E., Silva Aguirre, V., Christensen-Dalsgaard, J., et al. 2017, A&A, 608, A112
Önehag, A., Gustafsson, B., & Korn, A. 2014, A&A, 562, A102
Pasquini, L., Biazzo, K., Bonifacio, P., Randich, S., & Bedin, L. R. 2008, A&A, 489, 677
Piatti, A. E., Clariá, J. J., Bica, E., Geisler, D., & Minniti, D. 1998, AJ, 116, 801
Ramírez, I., Meléndez, J., & Asplund, M. 2009, A&A, 508, L17
Ramírez, I., Meléndez, J., & Asplund, M. 2014a, A&A, 561, A7
Ramírez, I., Meléndez, J., Bean, J., et al. 2014b, A&A, 572, A48
Randich, S., Sestito, P., Primas, F., Pallavicini, R., & Pasquini, L. 2006, A&A, 450, 557
Randich, S., Gilmore, G., & Gaia-ESO Consortium 2013, The Messenger, 154, 47
Randich, S., Tognelli, E., Jackson, R., et al. 2018, A&A, 612, A99
Romano, D., Karakas, A. I., Tosi, M., & Matteucci, F. 2010, A&A, 522, A32
Rosén, L., Kochukhov, O., Hackman, T., & Lehtinen, J. 2016, A&A, 593, A35
Salaris, M., Chieffi, A., & Straniero, O. 1993, ApJ, 414, 580
Salaris, M., Weiss, A., & Percival, S. M. 2004, A&A, 414, 163
Schönrich, R., Binney, J., & Dehnen, W. 2010, MNRAS, 403, 1829
Sharma, S., Pandey, A. K., Ogura, K., et al. 2006, AJ, 132, 1669

Shingles, L. J., Doherty, C. L., Karakas, A. I., et al. 2015, MNRAS, 452, 2804
Skúladóttir, Á., Hansen, C. J., Salvadori, S., & Choplin, A. 2019, A&A, 631, A171
Slumstrup, D., Grundahl, F., Brogaard, K., et al. 2017, A&A, 604, L8
Sneden, C. 1973, ApJ, 184, 839
Soderblom, D. R. 2010, ARA&A, 48, 581
Soderblom, D. R., Hillenbrand, L. A., Jeffries, R. D., Mamajek, E. E., & Naylor, T. 2014, Protostars and Planets VI, 219
Spada, F., Demarque, P., Kim, Y. C., Boyajian, T. S., & Brewer, J. M. 2017, ApJ, 838, 161
Spina, L., Meléndez, J., Karakas, A. I., et al. 2016, A&A, 593, A125
Spina, L., Meléndez, J., Karakas, A. I., et al. 2018, MNRAS, 474, 2580
Stonkute, E., Koposov, S.E., & Howes, L.M. 2016, MNRAS, 460
Titarenko, A., Recio-Blanco, A., de Laverny, P., Hayden, M., & Guiglion, G. 2019, A&A, 622, A59
Tucci Maia, M., Ramírez, I., Meléndez, J., et al. 2016, A&A, 590, A32

[1] Dipartimento di Fisica e Astronomia, Università degli Studi di Firenze, via G. Sansone 1, 50019 Sesto Fiorentino (Firenze), Italy
e-mail: casali@arcetri.astro.it
[2] INAF – Osservatorio Astrofisico di Arcetri, Largo E. Fermi 5, 50125 Florence, Italy
[3] Monash Centre for Astrophysics, School of Physics and Astronomy, Monash University, VIC 3800, Australia
[4] Centre for Astrophysics Research, University of Hertfordshire, College Lane, Hatfield AL10 9AB, UK
[5] Institute of Astronomy, Madingley Road, University of Cambridge CB3 0HA, UK
[6] McWilliams Center for Cosmology, Department of Physics, Carnegie Mellon University, 5000 Forbes Avenue, Pittsburgh, PA 15213, USA
[7] Dipartimento di Fisica e Astronomia Galileo Galilei, Vicolo Osservatorio 3, 35122 Padova, Italy
[8] Dipartimento di Fisica, Università di Pisa, Largo Bruno Pontecorvo 3, 56127 Pisa, Italy
[9] Instituto de Astrofísica e Ciências do Espaço, Universidade do Porto, CAUP, Rua das Estrelas, 4150-7 Porto, Portugal
[10] Departamento de Ciencias Fisicas, Universidad Andres Bello, Fernandez Concha 700, Las Condes, Santiago, Chile
[11] Núcleo de Astronomía, Facultad de Ingeniería, Universidad Diego Portales, Av. Ejército 441, Santiago, Chile
[12] INAF – Osservatorio di Astrofisica e Scienza dello Spazio di Bologna, via Gobetti 93/3, 40129 Bologna, Italy
[13] INAF – Padova Observatory, Vicolo dell'Osservatorio 5, 35122 Padova, Italy
[14] Instituto de Astrofísica de Andalucía-CSIC, Apdo. 3004, 18080 Granada, Spain
[15] Lund Observatory, Department of Astronomy and Theoretical Physics, Box 43 221 00 Lund, Sweden
[16] Rome Astronomical Observatory (OAR), Via di Frascati, 33, 00044 Monte Porzio Catone, Italy
[17] Institute of Theoretical Physics and Astronomy, Vilnius University, Saulėtekio av. 3, 10257 Vilnius, Lithuania
[18] ARC Centre of Excellence for All Sky Astrophysics in 3 Dimensions (ASTRO 3D), Sydney, Australia
[19] School of Physics, University of New South Wales, Sydney, NSW 2052, Australia
[20] Nicolaus Copernicus Astronomical Center, Polish Academy of Sciences, ul. Bartycka 18, 00-716 Warsaw, Poland
[21] Observational Astrophysics, Division of Astronomy and Space Physics, Department of Physics and Astronomy, Uppsala University, Box 516, 751 20 Uppsala, Sweden
[22] Laboratoire Lagrange (UMR7293), Université de Nice Sophia Antipolis, CNRS,Observatoire de la Côte d'Azur, CS 34229, 06304 Nice Cedex 4, France
[23] Astrophysics Group, Research Institute for the Environment, Physical Sciences and Applied Mathematics, Keele University, Keele, Staffordshire ST5 5BG, UK
[24] Instituto de Física y Astronomía, Facultad de Ciencias, Universidad de Valparaíso, Av. Gran Bretaña 1111, Valparaíso, Chile
[25] INFN, Sezione di Pisa, Largo Bruno Pontecorvo 3, 56127 Pisa, Italy